Measurement 248 (2025) 116961

Contents lists available at ScienceDirect

Measurement

journal homepage: www.elsevier.com/locate/measurement

On the measurement of resonance frequency of nanoclay-reinforced concrete shell structures validated by experimental datasets via artificial intelligence technique and mathematical modeling

Zhonghong Li [a], Yang Bing [a,*], Suming Chen [a], Mohammed El-Meligy [b,c], Mubariz Garayev [d]

[a] School of Architectural Engineering, Chongqing Chemical Industry Vocational College, Chongqing 401228, China
[b] Jadara University Research Center, Jadara University, PO Box 733, Irbid, Jordan
[c] Applied Science Research Center, Applied Science Private University, Amman, Jordan
[d] Department of Mathematics, College of Science, King Saud University, P.O Box 2455, Riyadh, Saudi Arabia

ARTICLE INFO

Keywords:
Resonance frequency measurement
Concrete cylindrical shell
Viscoelastic foundation
Nanoclay reinforcement
Airflow pressure
DNN-fuzzy algorithm

ABSTRACT

This study measures the resonance frequency and relative frequency change of concrete cylindrical shells reinforced with nanoclay and resting on viscoelastic foundations under combined in-plane and airflow pressures. Advanced mathematical modeling is employed to measure the natural frequencies of the system, incorporating the effects of nanoclay reinforcement on material properties. The viscoelastic foundation is represented using a Kelvin-Voigt framework, accurately modeling the time-dependent behavior of the substrate. Parameterized simulations are conducted to measure the structural response, focusing on the influence of varying nanoclay content and in-plane pressures on frequency characteristics. The mathematical model is validated by measuring its performance against experimental datasets from the literature and by integrating a deep neural network (DNN) with a fuzzy algorithm for computational verification. Results reveal that nanoclay reinforcement significantly measures as an enhancement in the stiffness and stability of the shell, resulting in increased natural frequencies. Additionally, the mechanical effects induced by the interplay of in-plane and airflow pressures are captured effectively through the proposed measurement framework. This research establishes a robust methodology for the analysis of reinforced cylindrical shells, providing key insights into material and structural design optimization for aeronautical and civil engineering applications. The integration of a DNN-fuzzy algorithm enhances the reliability of the measurement outcomes, setting the foundation for advanced predictive tools in structural dynamics. These findings offer valuable measures to understand reinforced shell behavior under complex pressure conditions, facilitating improved design strategies.

1. Introduction

Nanoclay reinforcement plays a critical role in engineering due to its ability to enhance material properties at a nanoscale level [1,2]. These materials are composed of layered silicates with high aspect ratios, offering a unique combination of mechanical, thermal, and barrier enhancements [3]. When incorporated into polymer matrices, nanoclays improve stiffness, strength, and resistance to deformation without significantly increasing the material's weight [4]. Their nanoscale dimensions enable large interfacial areas, which promote effective load transfer and interfacial bonding [5]. Additionally, nanoclay-reinforced composites exhibit superior thermal stability and flame retardancy, making them ideal for applications in the aerospace, automotive, and construction industries [6]. Their exceptional barrier properties against gases and liquids also make them indispensable in packaging technologies [7]. Nanoclays are cost-effective and environmentally friendly, providing engineers with a sustainable alternative for material enhancement [8]. The tailoring of nanoclay properties through surface modification further allows for customized solutions tailored to specific engineering challenges [9]. Moreover, their dispersibility in various matrices supports versatile applications across diverse fields [10]. Overall, nanoclay reinforcement is a cornerstone of modern materials engineering, contributing significantly to advancements in lightweight and high-performance composite materials [11].

Concrete structures are fundamental to engineering due to their durability, versatility, and ability to withstand significant loads [12]. As

* Corresponding author.
E-mail address: 1114052603@qq.com (Y. Bing).

https://doi.org/10.1016/j.measurement.2025.116961
Received 8 October 2024; Received in revised form 4 February 2025; Accepted 5 February 2025
Available online 7 February 2025

a composite material, concrete is widely used in the construction of buildings, bridges, dams, and infrastructure, offering engineers a cost-effective and sustainable option for large-scale projects [13]. Its excellent compressive strength and adaptability to various forms enable the design of complex and resilient structures [14]. Additionally, concrete's compatibility with reinforcing materials like steel enhances its tensile strength, allowing it to meet diverse structural demands [15]. The longevity and minimal maintenance requirements of concrete structures make them an essential component in addressing the growing global need for sustainable and reliable infrastructure [16].

Natural frequency analysis is a critical aspect of structural engineering, as it helps engineers understand how structures respond to dynamic loads and vibrational forces [17]. Every structure has inherent natural frequencies, and resonance occurs when external vibrations match these frequencies, potentially causing catastrophic failure [18]. By analyzing natural frequencies, engineers can predict and mitigate resonance effects, ensuring the structural integrity and safety of buildings, bridges, and machinery [19]. This analysis is especially vital in seismic and wind engineering, where dynamic forces can have a profound impact [20]. It also supports the optimization of materials and design, balancing strength and flexibility to minimize vibrational amplitudes [21]. Natural frequency analysis is essential in designing structures that interact with moving components [22]. Additionally, it informs decisions about damping systems and isolation techniques to reduce vibrational impacts [23]. Advances in computational tools have enabled engineers to perform accurate modal analysis, even for complex geometries [24]. The results of such analyses contribute to the development of safer and more resilient infrastructure [25]. Ultimately, natural frequency analysis is indispensable for creating designs that ensure long-term performance, reliability, and compliance with safety standards [26].

Machine learning (ML) algorithms are transforming engineering by enabling the analysis of complex data and the development of intelligent, predictive systems [27]. Engineers leverage ML to optimize design processes, automate decision-making, and enhance the efficiency of manufacturing and operations [28]. These algorithms identify patterns and insights from vast datasets, surpassing traditional computational methods in accuracy and speed [29]. In structural engineering, ML aids in predicting material behaviors and failure modes, improving safety and reliability [30]. Electrical engineers use ML for optimizing power systems, predictive maintenance, and smart grid technologies [31]. Similarly, ML in mechanical engineering facilitates robotics, control systems, and advanced simulations [32]. The integration of ML algorithms accelerates innovation by reducing experimentation costs and time, fostering data-driven design and prototyping [33]. Furthermore, ML enhances the precision of diagnostics and monitoring in various engineering systems, enabling proactive responses to potential issues [34]. Advances in ML frameworks and tools empower engineers to tackle multidisciplinary challenges, from renewable energy optimization to autonomous systems [35]. Ultimately, ML algorithms are indispensable for modern engineering, driving advancements that reshape industries and improve the quality of life globally [36].

This work examines the resonance frequency and relative frequency variation of concrete cylindrical shells reinforced with nanoclay, supported by viscoelastic foundations, under the influence of combined in-plane and airflow forces. The inherent frequencies of the system are studied using sophisticated mathematical modeling, taking into account the effect of nanoclay reinforcement on material characteristics. The viscoelastic foundation was represented using a Kelvin-Voigt model, which accounts for the time-dependent characteristics of the viscoelastic substrate. The structural response is measured by parameterized simulations, emphasizing the effect of different nanoclay concentrations and in-plane pressures on frequency characteristics. The mathematical model is also validated using existing experimental datasets from the literature and a deep neural network combined with a fuzzy algorithm, offering a strong computational method for corroborating analytical findings. The results indicate that nanoclay reinforcement significantly improves the stiffness and stability of the shell, resulting in increased natural frequencies. Moreover, the interplay between in-plane pressure and airflow pressure generates mechanical effects that are precisely represented by the suggested model. This study presents a thorough technique for the analysis of reinforced cylindrical shells, with ramifications for design optimization in aeronautical and civil engineering fields. The use of the DNN-fuzzy method for result validation guarantees the trustworthiness of outputs, facilitating the development of sophisticated forecasting tools in structural dynamics. These results boost the comprehension of reinforced shell behavior under intricate pressure situations, facilitating improved material and structural design.

2. Mathematical modeling

2.1. Material properties of the nanoclay composites reinforced concrete shell structure

Currently, a frequently used material in industry is a composite composed of polymers. These materials are attracting significant attention in the aerospace, military, and aviation industries because of their exceptional mechanical properties and substantial weight reduction in structural design. Composite materials are distinguished from traditional metallic alloys by their exceptional attributes, including a high strength-to-weight ratio, fatigue resistance, and wear resistance [37]. Furthermore, this study considers a cylindrical shell denoted by the letter L. Fig. 1 illustrates that the mean radius is denoted as R and the shell thickness as h. The radial coordinate is denoted as r, while $\mathscr{X}$ represents the axial direction. The circumferential angle θ defines the shell's angular position.

2.2. Elasticity modulus using the Halpin-Tsai model

The elastic modulus of composite materials, including nanoclay-reinforced composites, is often estimated using the Halpin-Tsai model. This model considers the distribution, shape, and direction of the reinforcement inside the matrix. The effective Young's modulus, E_c, of a nanoclay-reinforced composite may be estimated as follows:

$$E_c = E_m \times ((1 + 2\eta W_{NC})/(1 - \eta W_{NC})) \tag{1}$$

where:

E_c = Effective Young's modulus of the composite.

E_m = Young's modulus of the matrix material.

W_{NC} = Volume fraction of the nanoclay.η = Reinforcement efficiency parameter, defined as:

$$\eta = ((E_f/E_m) - 1)/((E_f/E_m) - 2\zeta), \tag{2}$$

where:

E_f = Young's modulus of the nanoclay.

$\zeta = A$ parameter depending on the shape and orientation of the nanoclay particles.

2.3. Other material properties

The Poisson's ratio of the composite can be estimated as:

$$\vartheta_c = \vartheta_m \times (1 - W_{NC}) + \vartheta_f \times W_{NC}, \tag{3}$$

where:

ϑ_c= Poisson's ratio of the composite.

ϑ_m= Poisson's ratio of the matrix.

ϑ_f= Poisson's ratio of the nanoclay. The density of the composite is given by:

$$\rho_c = \rho_m \times (1 - W_{NC}) + \rho_f \times W_{NC}, \tag{4}$$

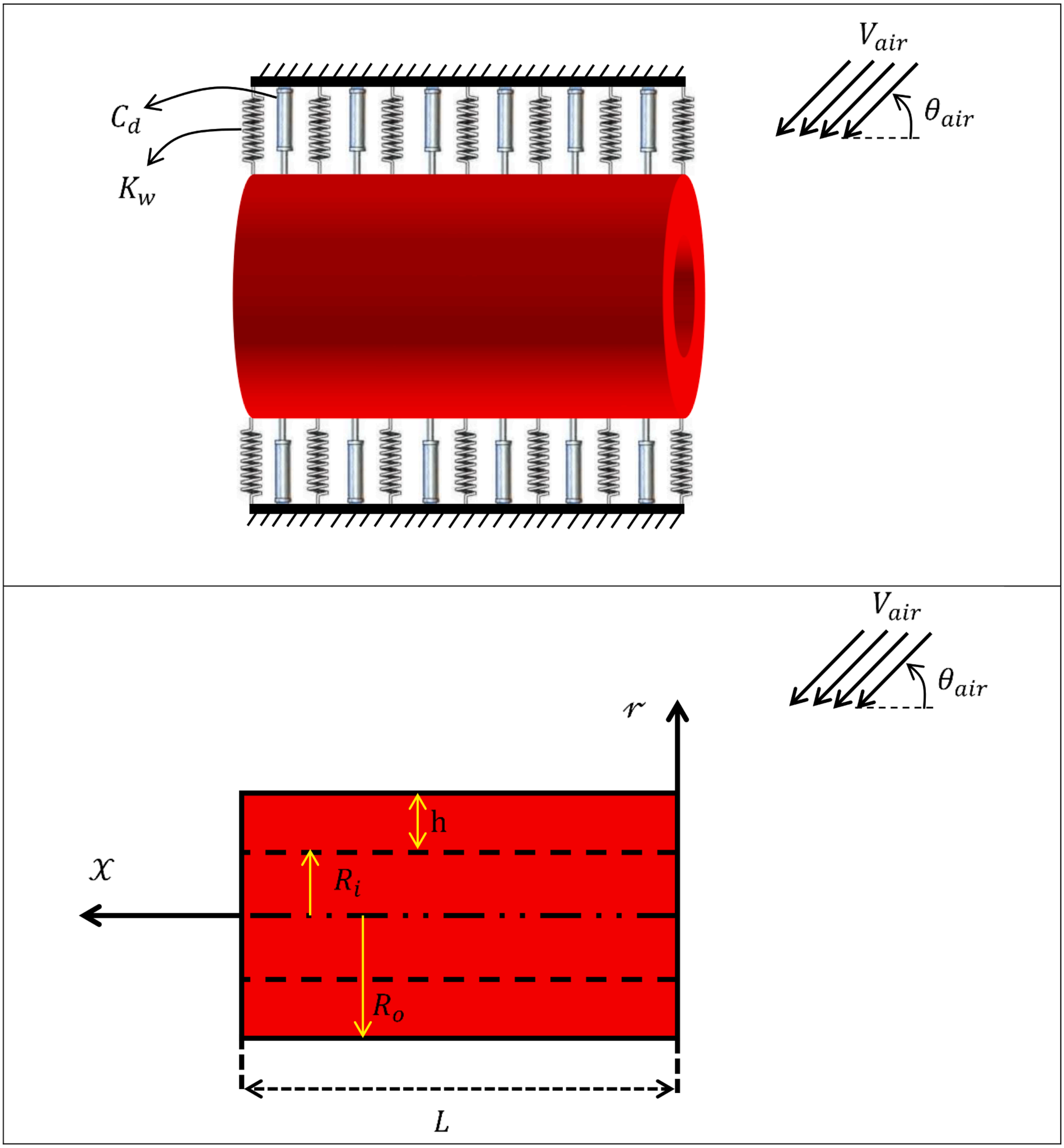

Fig. 1. Geometry and coordinate system of a concrete shell reinforced by nanoclay under airflow pressure.

where:

ρ_c = Density of the composite.
ρ_m = Density of the matrix.
ρ_f = Density of the nanoclay.

2.4. Distribution pattern of nanoclay along with thickness direction

The distribution of nanoclay may significantly influence the mechanical, thermal, and barrier properties of a composite material. The volume fraction, defined as the ratio of nanoclay volume to the total volume of the composite material, is often used to evaluate the impact of nanoclay dispersion. The role of nanoclay dispersion varies with volume percentage in several orientations, including thickness and in-plane directions.

$$PatternO : V_{NC}(r) = 2\left(1-2\frac{\left|r-\left(R_i+\frac{h}{2}\right)\right|}{h}\right)V^*_{NC}, \tag{5a}$$

$$PatternUD : V_{NC}(r) = V^*_{NC} \tag{5b}$$

$$PatternX : V_{NC}(r) = 4\frac{\left|r-\left(R_i+\frac{h}{2}\right)\right|}{h}V^*_{NC}, \tag{5c}$$

The total volume % of nanoclays is represented by V^*_{NC}. It stays stable and unaltered by the dispersions of nanoclays. This may be articulated as follows:

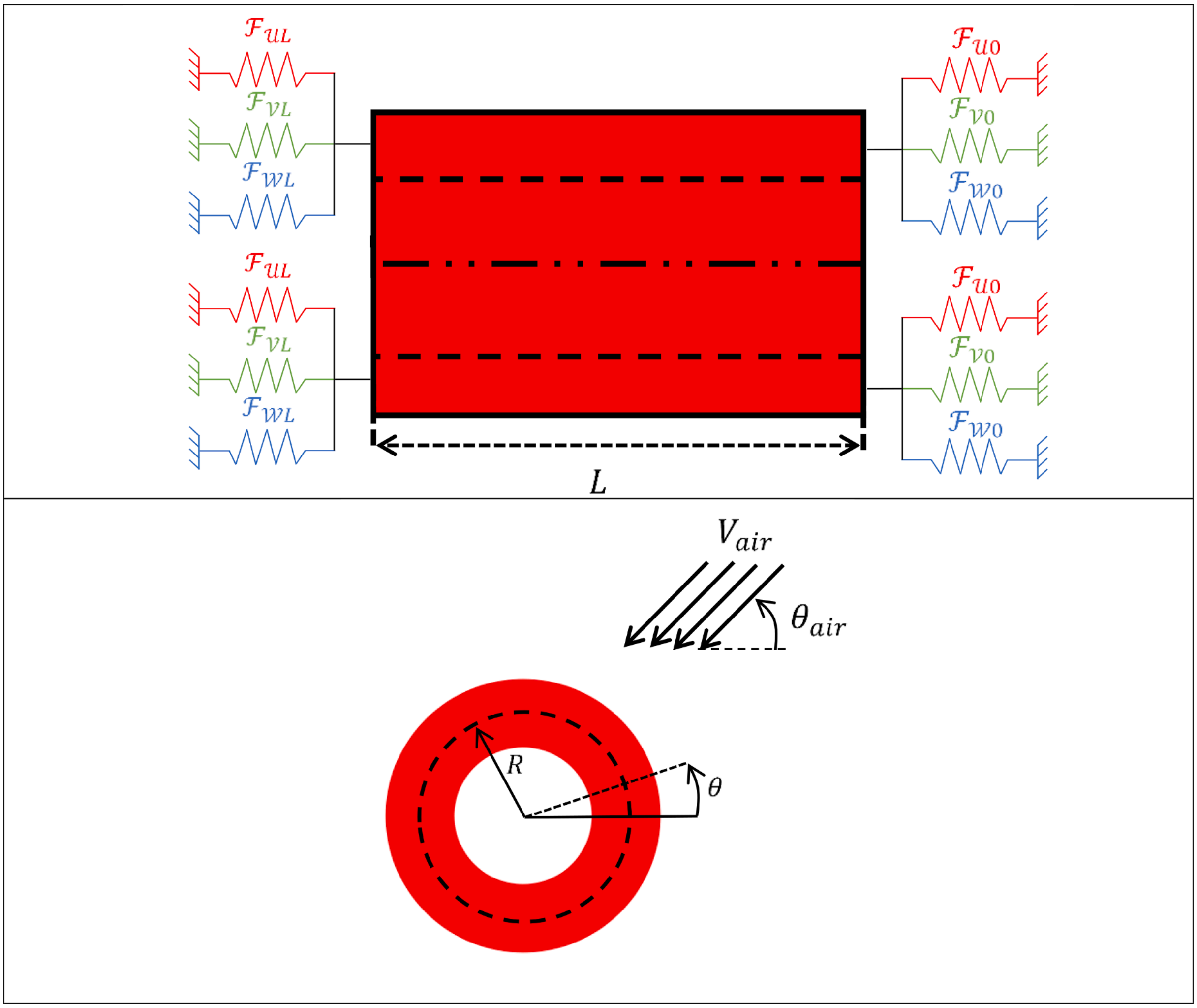

Fig. 1. (*continued*).

$$V^*_{NC} = \frac{W_{NC}}{W_{NC} + \rho_c/\rho_m - W_{NC}\rho_c/\rho_m}. \tag{6}$$

Various distribution patterns of nanoclays are shown in Fig. 2.

The properties of the materials used are presented in Table 1.

Table 1
Mechanical characteristics of the two constituents of the matrix and the reinforcement [38].

Property name	Matrix	Nanoclay
Modulus of elasticity (E) [GPa]	25	178
Density (ρ) [kg/m^3]	2300	2580
Poisson's ratio (ϑ)	0.2	0.25

2.5. Kinematic relations and energy expressions

The linear strain–displacement relationships may be elucidated using the three-dimensional shell theory of elasticity as

$$\mathscr{E}_{\mathscr{X}} = \frac{\partial \mathscr{U}}{\partial \mathscr{X}}, \mathscr{E}_{\theta} = \frac{\partial \mathscr{V}}{\mathscr{r}\partial\theta} + \frac{\mathscr{W}}{\mathscr{r}}, \mathscr{E}_{\mathscr{r}} = \frac{\partial \mathscr{W}}{\partial \mathscr{r}}, \tag{7a}$$

$$\gamma_{\theta\mathscr{r}} = \frac{\partial \mathscr{W}}{\mathscr{r}\partial\theta} + \frac{\partial \mathscr{V}}{\partial \mathscr{r}} - \frac{\mathscr{V}}{\mathscr{r}}, \gamma_{\mathscr{X}\mathscr{r}} = \frac{\partial \mathscr{U}}{\partial \mathscr{r}} + \frac{\partial \mathscr{W}}{\partial \mathscr{X}}, \gamma_{\mathscr{X}\theta} = \frac{\partial \mathscr{U}}{\mathscr{r}\partial\theta} + \frac{\partial \mathscr{V}}{\partial \mathscr{X}}. \tag{7b}$$

$\mathscr{E}_{\mathscr{X}}$, $\mathscr{E}_{\theta}$ and $\mathscr{E}_{\mathscr{r}}$ denote the normal strains along the respective directions; $\gamma_{\theta\mathscr{r}}$, $\gamma_{\mathscr{X}\mathscr{r}}$ and $\gamma_{\mathscr{X}\theta}$ signify the shear strains; and $\mathscr{U}$, $\mathscr{V}$ and $\mathscr{W}$ represent the displacement components in the $\mathscr{X}$ (axial), θ(circumferential), and $\mathscr{r}$ (radial) directions. According to Hooke's law, the comprehensive stress–strain relationships may be articulated as

$$\sigma_{\mathscr{X}} = \mathscr{G}_{11}\mathscr{E}_{\mathscr{X}} + \mathscr{G}_{12}\mathscr{E}_{\theta} + \mathscr{G}_{13}\mathscr{E}_{\mathscr{r}}, \tag{8a}$$

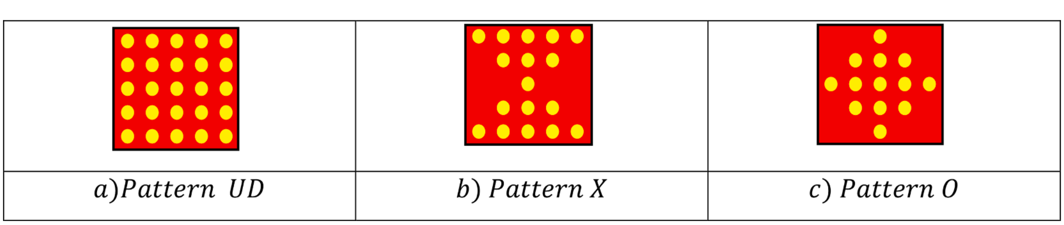

Fig. 2. Various distribution patterns of nanoclays.

$$\sigma_\theta = \mathcal{G}_{12}\mathcal{E}_{\mathcal{X}} + \mathcal{G}_{22}\mathcal{E}_\theta + \mathcal{G}_{23}\mathcal{E}_{r}, \tag{8b}$$

$$\sigma_{r} = \mathcal{G}_{13}\mathcal{E}_{\mathcal{X}} + \mathcal{G}_{23}\mathcal{E}_\theta + \mathcal{G}_{33}\mathcal{E}_{r}, \tag{8c}$$

$$\tau_{\theta r} = \mathcal{G}_{44}\gamma_{\theta r}, \tag{8d}$$

$$\tau_{\mathcal{X}r} = \mathcal{G}_{55}\gamma_{\mathcal{X}r}, \tag{8e}$$

$$\tau_{\mathcal{X}\theta} = \mathcal{G}_{66}\gamma_{\mathcal{X}\theta}. \tag{8f}$$

where $\sigma_{\mathcal{X}}$, σ_θ and σ_{r} denote normal stresses; $\tau_{\theta r}$, $\tau_{\mathcal{X}r}$ and $\tau_{\mathcal{X}\theta}$ indicate shear stresses; $\mathcal{G}_{ij}(i,j = 1-6)$ represent the elastic constants, which may be expressed as

$$\mathcal{G}_{11} = \mathcal{G}_{22} = \mathcal{G}_{33} = \frac{E_c(1-\vartheta_c)}{(1+\vartheta_c)(1-2\vartheta_c)}, \mathcal{G}_{12} = \mathcal{G}_{13} = \mathcal{G}_{23} = \frac{\vartheta_c E_c}{(1+\vartheta_c)(1-2\vartheta_c)}, \tag{9a}$$

$$\mathcal{G}_{44} = \mathcal{G}_{55} = \mathcal{G}_{66} = \frac{E_c}{2(1+\vartheta_c)}. \tag{9b}$$

According to the kinematic relations, the strain energy U_V of the composite structure is expressed as follows

$$\begin{aligned} U_V &= \frac{1}{2}\int_V (\sigma_{\mathcal{X}}\mathcal{E}_{\mathcal{X}} + \sigma_{r}\mathcal{E}_{r} + \sigma_\theta\mathcal{E}_\theta + \tau_{\theta r}\gamma_{\theta r} + \tau_{\mathcal{X}r}\gamma_{\mathcal{X}r} + \tau_{\mathcal{X}\theta}\gamma_{\mathcal{X}\theta})dV \\ &= \frac{1}{2}\int_V \left\{ \mathcal{G}_{11}\left(\frac{\partial \mathcal{U}}{\partial \mathcal{X}}\right)^2 + 2\mathcal{G}_{12}\frac{\partial \mathcal{U}}{\partial \mathcal{X}}\left(\frac{\partial \mathcal{V}}{r\partial\theta} + \frac{\mathcal{W}}{r}\right) + 2\mathcal{G}_{13}\frac{\partial \mathcal{U}}{\partial \mathcal{X}}\frac{\partial \mathcal{W}}{\partial r} + \mathcal{G}_{22}\left(\frac{\partial \mathcal{V}}{r\partial\theta} + \frac{\mathcal{W}}{r}\right)^2 + 2\mathcal{G}_{23}\left(\frac{\partial \mathcal{V}}{r\partial\theta} \right.\right. \\ &\left.\left. + \frac{\mathcal{W}}{r}\right)\frac{\partial \mathcal{W}}{\partial r} + \mathcal{G}_{33}\left(\frac{\partial \mathcal{W}}{\partial r}\right)^2 + \mathcal{G}_{44}\left(\frac{\partial \mathcal{W}}{r\partial\theta} + \frac{\partial \mathcal{V}}{\partial r} - \frac{\mathcal{V}}{r}\right)^2 + \mathcal{G}_{55}\left(\frac{\partial \mathcal{U}}{\partial r} + \frac{\partial \mathcal{W}}{\partial \mathcal{X}}\right)^2 + \mathcal{G}_{66}\left(\frac{\partial \mathcal{U}}{r\partial\theta} + \frac{\partial \mathcal{V}}{\partial \mathcal{X}}\right)^2 \right\}dV. \end{aligned} \tag{10}$$

This research employs a collection of constantly distributed boundary springs to imitate the boundary conditions [39].

One may produce diverse boundary conditions by altering the values of each stiffness. The conserved potential energy U_S of the boundary springs is

$$U_S = \frac{1}{2}\int_{R_i}^{R_o}\int_0^{2\pi}\left\{ \left[\mathcal{F}_{\mathcal{U}0}\mathcal{U}^2 + \mathcal{F}_{\mathcal{V}0}\mathcal{V}^2 + \mathcal{F}_{\mathcal{W}0}\mathcal{W}^2\right]|_{\mathcal{X}=0} + \left[\mathcal{F}_{\mathcal{U}L}\mathcal{U}^2 + \mathcal{F}_{\mathcal{V}L}\mathcal{V}^2 + \mathcal{F}_{\mathcal{W}L}\mathcal{W}^2\right]|_{\mathcal{X}=L}\right\} r d\theta dr. \tag{11}$$

Three sets of linear springs with stiffnesses $\mathcal{F}_{\mathcal{U}0}$, $\mathcal{F}_{\mathcal{V}0}$ and $\mathcal{F}_{\mathcal{W}0}$ (or $\mathcal{F}_{\mathcal{U}L}$, $\mathcal{F}_{\mathcal{V}L}$ and $\mathcal{F}_{\mathcal{W}L}$) are positioned at edge $\mathcal{X} = 0$ (or edge $\mathcal{X} = L$). Three sets of linear springs with stiffnesses for various boundary conditions, such as simply-supported (S) and clamped (C), can be obtained by appropriately setting the values of the spring stiffness. Their value is dependent on the convergence study of the results that will be presented in the convergence study section. Mechanical stress and viscoelastic foundations are considered, as previously mentioned. The following expression denotes the potential energy linked to the three elastic foundations U_F:

$$U_{F,WP} = \frac{1}{2}\int_0^L\int_0^{2\pi}\left\{K_w\mathcal{W}^2 + C_d\left(\frac{\partial \mathcal{W}}{\partial t}\right)^2\right\}|_{r=R_o} R_o d\theta d\mathcal{X}, \tag{12a}$$

$$U_{F,P} = \frac{1}{2}\int_0^L\int_0^{2\pi}\left\{P^*\left[\left(\frac{\partial \mathcal{W}}{\partial \mathcal{X}}\right)^2 + \left(\frac{\partial \mathcal{W}}{r\partial\theta}\right)^2\right]\right\}|_{r=R_o} R_o d\theta d\mathcal{X}. \tag{12b}$$

$U_{F,WP}$ denotes the potential energy associated with visco-elastic foundations, whereas $U_{F,P}$ signifies the potential energy related to mechanical load. Also, P^* shows the pressure. Furthermore, the kinetic energy T may be represented as

$$T = \int_{R_i}^{R_o}\int_0^{2\pi}\int_0^L \frac{\rho_c}{2}\left\{\left(\frac{\partial \mathcal{U}}{\partial t}\right)^2 + \left(\frac{\partial \mathcal{V}}{\partial t}\right)^2 + \left(\frac{\partial \mathcal{W}}{\partial t}\right)^2\right\} r d\mathcal{X} d\theta dr. \tag{13}$$

Furthermore, to effectuate a work alteration by airflow pressure pressure, $U_{F,V}$ may be articulated as follows:

$$U_{F,V} = -\frac{1}{2}\int_0^L\int_0^{2\pi}\left\{q\left(\frac{\partial \mathcal{W}}{\partial \mathcal{X}}\right)^2\right\}|_{r=R_o} R_o d\theta d\mathcal{X}. \tag{14}$$

In which:

$$q = \frac{1}{2}\rho_{air}V_{air}^2\sin(\theta_{air}). \tag{15}$$

In this context, θ_{air} and V_{air} represent the wind attack angle and average wind speed, respectively, while the air density, ρ_{air}, is assumed to beρ_{air} $= 1.235$ [kg/m^3] [40].

2.6. Admissible displacement functions and unified solution

This section identifies six unique kinds of permissible functions for comparison. The recursive formulae of order i and variable $\mathbb{A}$ may be denoted as $\mathbb{B}_i(\mathbb{A})$. The intervals of $\mathbb{A}$ differ across distinct polynomials; hence, the following equations may be presented:

(1) Chebyshev polynomials of the first kind (Chebyshev I) [41]

$$\mathbb{B}_0(\mathfrak{Y}) = 1, \mathbb{B}_1(\mathfrak{Y}) = \mathfrak{Y}, \mathbb{B}_i(\mathfrak{Y}) = 2\mathfrak{Y}\mathbb{B}_{i-1}(\mathfrak{Y}) - \mathbb{B}_{i-2}(\mathfrak{Y}), i \geq 2, \mathfrak{Y} \in [-1,1]. \tag{16}$$

(2) Chebyshev polynomials of the second kind (Chebyshev II) [41]:

$$\mathbb{B}_0(\mathfrak{Y}) = 1, \mathbb{B}_1(\mathfrak{Y}) = 2\mathfrak{Y}, \mathbb{B}_i(\mathfrak{Y}) = 2\mathfrak{Y}\mathbb{B}_{i-1}(\mathfrak{Y}) - \mathbb{B}_{i-2}(\mathfrak{Y}), i \geq 2, \mathfrak{Y} \in [-1,1]. \tag{17}$$

(3) Legendre polynomials [41]:

$$\mathbb{B}_0(\mathfrak{Y}) = 1, \mathbb{B}_1(\mathfrak{Y}) = 2\mathfrak{Y}, \mathbb{B}_i(\mathfrak{Y}) = \frac{2i-1}{i}\mathfrak{Y}\mathbb{B}_{i-1}(\mathfrak{Y}) - \frac{(i-1)}{i}\mathbb{B}_{i-2}(\mathfrak{Y}), i \geq 2, \mathfrak{Y} \in [-1,1] \tag{18}$$

(4) Orthogonal polynomials [42]:

$$\mathbb{B}_0(\mathfrak{Y}) = 1, \mathbb{B}_i(\mathfrak{Y}) = \frac{\mathfrak{C}_i(\mathfrak{Y})}{\sqrt{\int_0^1 [\mathfrak{C}_i(\mathfrak{Y})]^2 d\mathfrak{Y}}}, i \geq 1. \tag{19}$$

where $\mathfrak{C}_i(\mathfrak{Y})$ are a set of polynomials which are orthogonal. The corresponding recursive formulas can be constructed below.

$$\begin{cases} \mathfrak{C}_1(Y) = 1, \mathfrak{C}_2(Y) = (Y - \mathfrak{X}_1)\mathfrak{C}_1(Y) \\ \mathfrak{C}_{i+1}(Y) = (Y - \mathfrak{X}_i)\mathfrak{C}_i(Y) - \mathfrak{T}_i\mathfrak{C}_{i-1}(Y), i \geq 2 \end{cases}, \mathfrak{Y} \in [0,1]. \tag{20}$$

where

$$\mathfrak{X}_i = \frac{\int_0^1 \mathfrak{Y}[\mathfrak{C}_i(\mathfrak{Y})]^2 d\mathfrak{Y}}{\int_0^1 [\mathfrak{C}_i(\mathfrak{Y})]^2 d\mathfrak{Y}}, \mathfrak{T}_i = \frac{\int_0^1 \mathfrak{Y}\mathfrak{C}_i(\mathfrak{Y})\mathfrak{C}_{i-1}(\mathfrak{Y})d\mathfrak{Y}}{\int_0^1 [\mathfrak{C}_{i-1}(\mathfrak{Y})]^2 d\mathfrak{Y}}. \tag{21}$$

(5) Modified Fourier series of the first kind (Modified Fourier I) [43]:

$$\mathbb{B}_i(\mathfrak{Y}) = \begin{cases} sin\frac{(i-3)\pi}{a}Y, 1 \leq i \leq 2 \\ cos\frac{(i-3)\pi}{a}Y, i > 2 \end{cases}. \tag{22}$$

$$u = \begin{Bmatrix} \mathbb{B}_0(\mathfrak{Y}_{\mathscr{X}})\mathbb{B}_0(\mathfrak{Y}_{r})cos(n\theta), \cdots, \mathbb{B}_{\overline{m}}(\mathfrak{Y}_{\mathscr{X}})\mathbb{B}_{\overline{n}}(\mathfrak{Y}_{r})cos(n\theta), \cdots, \mathbb{B}_M(\mathfrak{Y}_{\mathscr{X}})\mathbb{B}_N(\mathfrak{Y}_{r})cos(n\theta) \\ \mathbb{B}_0(\mathfrak{Y}_{\mathscr{X}})\mathbb{B}_0(\mathfrak{Y}_{r})sin(n\theta), \cdots, \mathbb{B}_{\overline{m}}(\mathfrak{Y}_{\mathscr{X}})\mathbb{B}_{\overline{n}}(\mathfrak{Y}_{r})sin(n\theta), \cdots, \mathbb{B}_M(\mathfrak{Y}_{\mathscr{X}})\mathbb{B}_N(\mathfrak{Y}_{r})sin(n\theta) \end{Bmatrix}, \tag{30a}$$

In $\mathscr{X}$ direction, $a = L$, $\mathbb{A} \in [0, L]$; in r direction, $a = h$, $\mathbb{A} \in [0, h]$. It is worth noting that when $i = 1$ and 2, two supplementary terms with sinusoidal form are exerted to assure the second derivatives of admissible functions.

(6) Modified Fourier series of the second kind (Modified Fourier II) [44]:

$$\mathbb{B}_1(\mathfrak{Y}) = \mathfrak{Y}\left(\frac{\mathfrak{Y}}{a} - 1\right)^2, \mathbb{B}_2(\mathfrak{Y}) = \frac{\mathfrak{Y}^2}{a}\left(\frac{\mathfrak{Y}}{a} - 1\right), \mathbb{B}_i(\mathfrak{Y}) = \cos\frac{(i-3)\pi}{a}\mathfrak{Y}, i \geq 3 \tag{23}$$

In $\mathscr{X}$ direction, $a = L$, $\mathbb{A} \in [0,L]$; in r direction, $a = h$, $\mathbb{A} \in [0,h]$. Again, two additional terms $\mathbb{B}_1$ and $\mathbb{B}_2$ are added to deal with any possible discontinuities. The displacement fields of the composite structures can be presented in a general form as [45]

$$\mathscr{U} = \sum_{\overline{m}=0}^{M}\sum_{\overline{n}=0}^{N}\mathbb{B}_{\overline{m}}(\mathfrak{Y}_{\mathscr{X}})\mathbb{B}_{\overline{n}}(\mathfrak{Y}_{r})\left[u^c_{\overline{mn}}\cos(n\theta) + u^s_{\overline{mn}}\sin(n\theta)\right]e^{i\omega t}, \tag{24a}$$

$$\mathscr{V} = \sum_{\overline{m}=0}^{M}\sum_{\overline{n}=0}^{N}\mathbb{B}_{\overline{m}}(\mathfrak{Y}_{\mathscr{X}})\mathbb{B}_{\overline{n}}(\mathfrak{Y}_{r})\left[v^c_{\overline{mn}}\cos(n\theta) + v^s_{\overline{mn}}sin(n\theta)\right]e^{i\omega t}, \tag{24b}$$

$$\mathscr{W} = \sum_{\overline{m}=0}^{M}\sum_{\overline{n}=0}^{N}\mathbb{B}_{\overline{m}}(\mathfrak{Y}_{\mathscr{X}})\mathbb{B}_{\overline{n}}(\mathfrak{Y}_{r})\left[w^c_{\overline{mn}}\cos(n\theta) + w^s_{\overline{mn}}\sin(n\theta)\right]e^{i\omega t}. \tag{24c}$$

where $u^c_{\overline{mn}}$, $u^s_{\overline{mn}}$, $v^c_{\overline{mn}}$, $v^s_{\overline{mn}}$, $w^c_{\overline{mn}}$ and $w^s_{\overline{mn}}$ are unknown expanded coefficients; M and N represent the maximum values of $\overline{m}$ and $\overline{n}$, respectively; n denotes the circumferential wave number; ω signifies the angular frequency, and t indicates time; $\mathbb{B}_{\overline{m}}(\mathfrak{Y}_{\mathscr{X}})$ and $\mathbb{B}_{\overline{n}}(\mathfrak{Y}_{r})$ are polynomials of degree $\overline{m}$ in the length direction and degree $\overline{n}$ in the radial direction, respectively. Their expressions are

$$\mathbb{B}_{\overline{m}} = [\mathbb{B}_0(\mathfrak{Y}_{\mathscr{X}}), \mathbb{B}_1(\mathfrak{Y}_{\mathscr{X}}), \cdots, \mathbb{B}_{\overline{m}}(\mathfrak{Y}_{\mathscr{X}}), \cdots, \mathbb{B}_M(\mathfrak{Y}_{\mathscr{X}})], \tag{25a}$$

$$\mathbb{B}_{\overline{n}} = [\mathbb{B}_0(\mathfrak{Y}_{r}), \mathbb{B}_1(\mathfrak{Y}_{r}), \cdots, \mathbb{B}_{\overline{n}}(\mathfrak{Y}_{r}), \cdots, \mathbb{B}_N(\mathfrak{Y}_{r})]. \tag{25b}$$

The $\mathfrak{Y}_{\mathscr{X}}$ and $\mathfrak{Y}_{r}$ are dimensionless coordinates in the $\mathscr{X}$ and r axes, respectively. They are derived from linear transformations of $\mathscr{X}$ and r, as distinct polynomials are specified across various intervals. Regarding Chebyshev polynomials of the first and second kinds, as well as Legendre polynomials

$$\mathfrak{Y}_{\mathscr{X}} = 2\mathscr{X}/L - 1, \mathfrak{Y}_{r} = 2r/h - 1, \tag{26}$$

For Orthogonal polynomials and Fourier-Bessel series

$$\mathfrak{Y}_{\mathscr{X}} = \frac{2\mathscr{X}}{L}, \mathfrak{Y}_{r} = \frac{2r}{h}, \tag{27}$$

For Modified Fourier I and II

$$\mathfrak{Y}_{\mathscr{X}} = \mathscr{X}, \mathfrak{Y}_{r} = r, \tag{28}$$

Then, the unified forms of admissible displacement functions can be represented as

$$\mathscr{U} = u \cdot \mathfrak{g}_{\mathscr{U}}, \mathscr{V} = v \cdot \mathfrak{g}_{\mathscr{V}}, \mathscr{W} = w \cdot \mathfrak{g}_{\mathscr{W}}, \tag{29}$$

where

$$v = w = u, \tag{30b}$$

$$\mathfrak{g}_{\mathscr{U}} = \left\{u^c_{00}, \cdots u^c_{\overline{mn}}, \cdots u^c_{MN}, u^s_{00}, \cdots u^s_{\overline{mn}}, \cdots u^s_{MN}\right\}e^{i\omega t}, \tag{30c}$$

$$\mathfrak{g}_{\mathscr{V}} = \left\{v^c_{00}, \cdots v^c_{\overline{mn}}, \cdots v^c_{MN}, v^s_{00}, \cdots v^s_{\overline{mn}}, \cdots v^s_{MN}\right\}e^{i\omega t}, \tag{30d}$$

$$\mathfrak{g}_{\mathscr{W}} = \left\{w^c_{00}, \cdots w^c_{\overline{mn}}, \cdots w^c_{MN}, w^s_{00}, \cdots w^s_{\overline{mn}}, \cdots w^s_{MN}\right\}e^{i\omega t}. \tag{30e}$$

The Rayleigh-Ritz method may now be used to execute the solution process. The Lagrangian energy function of the composite structure may be expressed as

$$\mathscr{L} = U_V + U_S + U_{F,WP} + U_{F,P} + U_{F,V} - T. \tag{31}$$

Subsequently, the function $\mathscr{L}$ is minimized about the unknown extended coefficients ϑ ($= u_{\overline{mn}}$, $v_{\overline{mn}}$ and $w_{\overline{mn}}$) as shown below.

$$\frac{\partial \mathscr{L}}{\partial \vartheta} = 0. \vartheta = u_{\overline{mn}}, v_{\overline{mn}}, w_{\overline{mn}} \tag{32}$$

Integrating Eqs. (24a), (24b), (24c), and (31) into Eq. (32) yields the motion equation of the composite structure.

$$(\mathscr{K} + i\omega\mathscr{C} - \omega^2\mathscr{M})\mathfrak{g} = 0. \tag{33}$$

M represents the mass matrices related to kinetic energy; $\mathscr{K}$ denotes the stiffness matrix connected with strain energy, potential energy inside the limits, elastic foundation, and mechanical load; $\mathfrak{g} = [\mathfrak{g}_{\mathscr{U}}, \mathfrak{g}_{\mathscr{V}}, \mathfrak{g}_{\mathscr{W}}]^T$.

in which:

$$\mathscr{C} = \begin{bmatrix} 0 & 0 & 0 \\ 0 & 0 & 0 \\ 0 & 0 & \mathscr{C}_{\mathscr{W}\mathscr{W}} \end{bmatrix}, \tag{34a}$$

$$\mathscr{C}_{\mathscr{W}\mathscr{W}} = \int\int \{C_d w^T w\}|_{r=R_o} R_o dS_3, \tag{34b}$$

$$\mathscr{M} = \begin{bmatrix} \mathscr{M}_{\mathscr{U}\mathscr{U}} & 0 & 0 \\ 0 & \mathscr{M}_{\mathscr{V}\mathscr{V}} & 0 \\ 0 & 0 & \mathscr{M}_{\mathscr{W}\mathscr{W}} \end{bmatrix}, \tag{34c}$$

$$\mathscr{M}_{\mathscr{U}\mathscr{U}} = \int\int\int \rho r u^{\mathrm{T}} u d\mathscr{v}, \mathscr{M}_{\mathscr{V}\mathscr{V}} = \int\int\int \rho r v^{\mathrm{T}} v d\mathscr{v}, \mathscr{M}_{\mathscr{W}\mathscr{W}} = \int\int\int \rho r w^{\mathrm{T}} w d\mathscr{v}, \tag{34d}$$

$$d\mathscr{v} = r dr d\theta d\mathscr{X}, \tag{34e}$$

$$\mathscr{K} = \begin{bmatrix} \mathscr{K}_{\mathscr{U}\mathscr{U}} & \mathscr{K}_{\mathscr{U}\mathscr{V}} & \mathscr{K}_{\mathscr{U}\mathscr{W}} \\ \mathscr{K}^{\mathrm{T}}_{\mathscr{U}\mathscr{V}} & \mathscr{K}_{\mathscr{V}\mathscr{V}} & \mathscr{K}_{\mathscr{V}\mathscr{W}} \\ \mathscr{K}^{\mathrm{T}}_{\mathscr{U}\mathscr{W}} & \mathscr{K}^{\mathrm{T}}_{\mathscr{V}\mathscr{W}} & \mathscr{K}_{\mathscr{W}\mathscr{W}} \end{bmatrix}, \tag{34f}$$

$$\mathscr{K}_{\mathscr{U}\mathscr{U}} = \int\int\int \left(\mathscr{G}_{11} r \frac{\partial u^T}{\partial \mathscr{X}} \frac{\partial u}{\partial \mathscr{X}} + \mathscr{G}_{55} r \frac{\partial u^T}{\partial r} \frac{\partial u}{\partial r} + \mathscr{G}_{66} \frac{1}{r} \frac{\partial u^T}{\partial \theta} \frac{\partial u}{\partial \theta} \right) d\mathscr{v} + \int\int \{ \mathscr{T}_{\mathscr{U}0} u^T u|_{\mathscr{X}=0} + \mathscr{T}_{\mathscr{U}L} u^T u|_{\mathscr{X}=L} \} dS_1, \tag{34g}$$

$$\mathscr{K}_{\mathscr{U}\mathscr{V}} = \int\int\int \left\{ \mathscr{G}_{12} \frac{\partial u^T}{\partial \mathscr{X}} \frac{\partial v}{\partial \theta} + \mathscr{G}_{66} \frac{\partial u^T}{\partial \theta} \frac{\partial v}{\partial \mathscr{X}} \right\} d\mathscr{v}, \tag{34h}$$

$$\mathscr{K}_{\mathscr{U}\mathscr{W}} = \int\int\int \left\{ \mathscr{G}_{12} \frac{\partial u^T}{\partial \mathscr{X}} w + \mathscr{G}_{13} r \frac{\partial u^T}{\partial \mathscr{X}} \frac{\partial w}{\partial r} + \mathscr{G}_{55} r \frac{\partial u^T}{\partial r} \frac{\partial w}{\partial r} \right\} d\mathscr{v}, \tag{34i}$$

$$\mathscr{K}_{\mathscr{V}\mathscr{V}} = \int\int\int \left\{ \frac{\mathscr{G}_{22}}{r} \frac{\partial v^T}{\partial \theta} \frac{\partial v}{\partial \theta} + \frac{\mathscr{G}_{44}}{r} v^T v + \mathscr{G}_{44} r \frac{\partial v^T}{\partial r} \frac{\partial v}{\partial r} + \mathscr{G}_{66} r \frac{\partial v^T}{\partial \mathscr{X}} \frac{\partial v}{\partial \mathscr{X}} - \mathscr{G}_{44} \left(v^T \frac{\partial v}{\partial r} + \frac{\partial v^T}{\partial r} v \right) \right\} d\mathscr{v} + \int\int \{ \mathscr{T}_{\mathscr{V}0} v^T v|_{\mathscr{X}=0} + \mathscr{T}_{\mathscr{V}L} v^T v|_{\mathscr{X}=L} \} dS_1, \tag{34j}$$

$$\mathscr{K}_{\mathscr{V}\mathscr{W}} = \int\int\int \left\{ \frac{\mathscr{G}_{22}}{r} \frac{\partial v^T}{\partial \theta} w + \mathscr{G}_{23} \frac{\partial v^T}{\partial \theta} \frac{\partial w}{\partial r} + \mathscr{G}_{44} \frac{\partial v^T}{\partial r} \frac{\partial w}{\partial \theta} - \frac{\mathscr{G}_{44}}{r} v^T \frac{\partial w}{\partial \theta} \right\} d\mathscr{v}, \tag{34k}$$

$$\mathscr{K}_{\mathscr{W}\mathscr{W}} = \int\int\int \left\{ \frac{\mathscr{G}_{22}}{r} w^T w + \mathscr{G}_{23} \left(w^T \frac{\partial w}{\partial r} + \frac{\partial w^T}{\partial r} w \right) + \mathscr{G}_{33} r \frac{\partial w^T}{\partial r} \frac{\partial w}{\partial r} + \frac{\mathscr{G}_{44}}{r} \frac{\partial w^T}{\partial \theta} \frac{\partial w}{\partial \theta} + \mathscr{G}_{55} r \frac{\partial w^T}{\partial \mathscr{X}} \frac{\partial w}{\partial \mathscr{X}} \right\} d\mathscr{v} + \int\int \{ \mathscr{T}_{\mathscr{W}0} w^T w|_{\mathscr{X}=0} + \mathscr{T}_{\mathscr{W}L} w^T w|_{\mathscr{X}=L} \} dS_1 + \int\int \{ K_W w^T w \}|_{r=R_o} R_o dS_3 + \int\int \left\{ P^* \frac{\partial w^T}{\partial \mathscr{X}} \frac{\partial w}{\partial \mathscr{X}} + \frac{\mathbb{B}}{r^2} \frac{\partial w^T}{\partial \theta} \frac{\partial w}{\partial \theta} \right\} \Big|_{r=R_o} \times R_o dS_3 + \int\int \left\{ q_r \frac{\partial w^T}{\partial \mathscr{X}} \frac{\partial w}{\partial \mathscr{X}} \right\} \Big|_{r=R_o} R_o dS_3, \tag{34l}$$

$$dS_1 = r dr d\theta, dS_3 = d\mathscr{X} d\theta, \tag{34m}$$

The dimensionless parameters may be calculated as follows:

$$K_w^* = \frac{K_w R^5}{E_m I}, P_0 = 1[MPa] C_d^* = \frac{C_d R^3}{\sqrt{E_m I}}. \tag{35}$$

3. Application of DNN-fuzzy algorithm to estimate the resonance frequency of nanoclay-reinforced concrete shell structures via appropriate datasets of mathematical modeling

The accurate estimation of the resonance frequency of nanoclay-reinforced concrete shell structures is critical for their stability and performance in various engineering applications. Traditional methods for determining resonance frequencies often involve labor-intensive experimental techniques or simplistic analytical models that may not capture the complex behavior of nanoclay-reinforced materials. Advances in computational methods, particularly in artificial intelligence and data-driven modeling, offer promising alternatives. This study explores the application of a Deep Neural Network (DNN) integrated with a fuzzy logic algorithm to estimate the resonance frequency of such structures. The hybrid DNN-fuzzy approach leverages the strengths of both techniques: the DNN's ability to model complex nonlinear relationships and fuzzy logic's capability to handle uncertainty and imprecision. A comprehensive dataset derived from mathematical simulations, validated by finite element analysis, forms the foundation of the predictive model. These simulations incorporate various influencing factors, such as shell geometry, material properties, and nanoclay content. The proposed methodology aims to enhance the precision and computational efficiency of resonance frequency predictions, providing engineers with a robust tool for design and analysis. The integration of DNN and fuzzy algorithms not only improves prediction accuracy but also offers insights into the key parameters affecting structural behavior, paving the way for advanced material and structural design practices. Here are the detailed steps of the DNN-Fuzzy algorithm for estimating the resonance frequency of nanoclay-reinforced concrete shell structures:

Step 1: Data Preparation

1. **Input Data Collection**:
   - Gather data on shell geometry.
   - Obtain material properties.
   - Include environmental factors or pressure conditions.
2. **Mathematical Simulation**:
   - Perform finite element analysis (FEA) or other mathematical simulations to generate a dataset of resonance frequencies corresponding to various structural and material configurations.
3. **Preprocessing**:
   - Normalize the dataset to a uniform scale for efficient DNN training.
   - Split the dataset into training, validation, and testing subsets.

Step 2: Deep Neural Network (DNN) Modeling.

4. **Network Design**:
   - Define the DNN architecture, including the number of layers, neurons, activation functions, and dropout rates.
5. **Training the DNN**:
   - Use the training dataset to optimize the network weights.
   - Employ a loss function and an optimizer for training.
6. **Validation**:
   - Monitor the performance on the validation dataset to fine-tune hyperparameters and prevent overfitting.

Step 3: Fuzzy Logic Integration

7. **Defining Fuzzy Rules**:
   - Develop a set of linguistic rules based on expert knowledge or dataset insights.
8. **Fuzzification**:
   - Convert numerical inputs into fuzzy variables using membership functions.
9. **Inference**:
   - Apply the fuzzy rules to estimate the resonance frequency range.
10. **Defuzzification**:
    - Convert the fuzzy output into a crisp value for resonance frequency estimation.

Step 4: DNN-Fuzzy Integration

11. **Combining DNN and Fuzzy Outputs**:
    - Use the DNN to predict a baseline resonance frequency.
    - Refine this prediction with the fuzzy logic system to incorporate uncertainty or imprecise data.

Step 5: Model Evaluation and Result Presentation

12. **Testing**:
    - Evaluate the combined DNN-fuzzy model on the testing dataset.
    - Compare predicted and actual resonance frequencies using performance metrics such as R-squared, RMSE, or MAE.
13. **Visualization**:
    - Present results using plots and error distributions.
14. **Sensitivity Analysis**:
    - Analyze the impact of key input variables on resonance frequency to interpret model behavior.
15. **Validation with Experimental Data**:
    - Where possible, validate predictions against experimental resonance frequency measurements.

The final algorithm provides accurate and interpretable resonance frequency estimates, demonstrating its applicability for design and optimization in nanoclay-reinforced concrete shell structures. The mathematical simulation for the DNN-Fuzzy algorithm involves two main components: (1) constructing the DNN model and (2) integrating fuzzy logic for refining predictions. Below is the mathematical framework:

3.1. Mathematical representation of the DNN component

- Input Representation

Let the input vector X contain n features:

$$X = [x_1, x_2, \cdots, x_n] \tag{36}$$

where $x_1, x_2, \cdots, x_n$ represent factors such as material properties, geometric parameters, and environmental conditions.

- Network Layers

The DNN consists of L layers, each defined by:

- Weight matrix $W^{(l)}$,
- Bias vector $b^{(l)}$,
- Activation function $f^{(l)}$.

The output of each layer l is computed as:

$$Z^{(l)} = f^{(l)}\left(W^{(l)}A^{(l-1)} + b^{(l)}\right) \tag{37}$$

where:

- $A^{(l-1)}$ is the output from the previous layer (with $A^{(0)} = X$).
- $Z^{(L)}$ gives the final DNN output $\widehat{y}_{DNN}$, the predicted resonance frequency.
- Loss Function

The training process minimizes a loss function, such as Mean Squared Error (MSE):

$$L = \frac{1}{m}\sum_{i=1}^{m}(y_i - \widehat{y}_i)^2 \tag{38}$$

where m is the number of training samples, y_i is the true value, and $\widehat{y}_i$ is the DNN output.

3.2. Mathematical representation of fuzzy logic component

- Fuzzification

Input features $X = [x_1, x_2, \cdots, x_n]$ are converted into fuzzy sets using membership functions. For a feature x_j, the membership function $\mu A(x_j)$ is defined as:

$$\mu A(x_j) = \left\{ \begin{array}{c} \frac{x_j - a}{b - a}, a \le x_j \le b \\ \frac{c - x_j}{c - b} b \le x_j \le c \\ 0, otherwise \end{array} \right\} \tag{39}$$

where $[a, b, c]$ are the parameters of the triangular membership function.

- Fuzzy Rules

Define fuzzy rules in the form:
IF $(x_1 is A_1)$ AND $(x_2 is A_2)$ THEN y is B.where A_1, A_2, and B are fuzzy sets.

- Inference

Combine multiple rules using fuzzy operators (e.g., min or product) to compute the fuzzy output. For R rules:

$$\mu B(y) = \max[\min(\mu A_1(x_1), \mu A_2(x_2), \cdots)] \tag{40}$$

- Defuzzification

Convert the fuzzy output into a crisp value $\widehat{y}_{Fuzzy}$ using the centroid method:

Table 2
Comparison of the natural frequencies of cylindrical shells with the published experimental dataset [46].

	Number of circumferential waves 5	7	9	11	13	15
Ref. [46] (EXP)	206.5573	163.3382	224.4411	326.5275	439.0462	588.0775
Present	207.2943	170.7712	231.1354	334.7115	460.6431	600.7371

Table 3
Convergence of non-dimensional frequencies on boundary spring stiffness with different boundary conditions considering $K_w^* = 1$, $C_d^* = 1$, $P^*/P_0 = 1$, $L/R = 10$, $R/h = 10$, $NCWF = 2[\%]$, clamped–clamped boundary conditions, $V_{air}/V_0 = 3$, $\theta_{air} = \pi/4$ and Pattern X.

Type of B.Cs	$\mathscr{T} = 10^{13}$	$\mathscr{T} = 10^{14}$	$\mathscr{T} = 10^{15}$	$\mathscr{T} = 10^{16}$	$\mathscr{T} = 10^{17}$	$\mathscr{T} = 10^{18}$
Simply-Simply B.Cs	0.1933	0.2448	0.2625	0.2625	0.2625	0.2625
Clamped-Clamped B.Cs	0.3325	0.4212	0.4515	0.4515	0.4515	0.4515

$$\widehat{y}_{Fuzzy} = \frac{\int y.\mu B(y)dy}{\int \mu B(y)dy} \tag{41}$$

3.3. Dnn-fuzzy integration

Combine the DNN output $\widehat{y}_{DNN}$ with the fuzzy logic output $\widehat{y}_{Fuzzy}$ to refine predictions:

$$\widehat{y} = \alpha\widehat{y}_{DNN} + (1-\alpha)\widehat{y}_{Fuzzy}. \tag{42}$$

where $\alpha \in [0, 1]$ is a weighting factor tuned during validation.

3.4. Model evaluation

Evaluate the final prediction $\widehat{y}$ against true resonance frequencies y using metrics such as:

- Root Mean Squared Error (RMSE):

$$RMSE = \sqrt{\frac{1}{m}\sum_{i=1}^{m}\left|y_i - \widehat{y}_i\right|^2}. \tag{43}$$

Coefficient of Determination (R^2)

$$R^2 = 1 - \frac{\sum_{i=1}^{m}\left(y_i - \widehat{y}_i\right)^2}{\sum_{i=1}^{m}\left(y_i - \overline{y}\right)^2}. \tag{44}$$

where $\overline{y}$ is the mean of true values. This framework integrates the predictive power of DNNs with the interpretability of fuzzy logic to provide accurate and robust resonance frequency estimates.

4. Results and discussion

4.1. Validation of the results via nondestructive testing

Table 2 compares the natural frequencies of a cylindrical shell for different numbers of circumferential waves based on experimental data [46] and present results. The circumferential wave numbers analyzed range from 5 to 15, covering values 5, 7, 9, 11, 13, and 15. The experimental data, denoted as Ref. [46], represent previously published results, while the present results provide newly computed values. The comparison evaluates the accuracy and reliability of the present model by observing deviations in frequencies at each wave number. For wave number 5, the experimental frequency is 206.5573, while the present result is slightly higher at 207.2943. At wave number 7, the values differ more significantly, with 163.3382 for Ref. [46] and 170.7712 for the present approach. Similarly, as the wave numbers increase, both datasets show higher frequencies, though the present model consistently predicts slightly larger values. At wave number 15, the experimental frequency is 588.0775, while the present result reaches 600.7371.

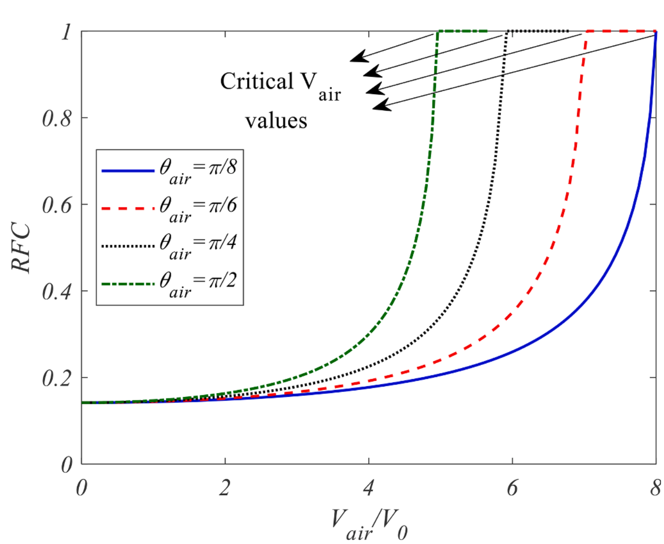

Fig. 3. The impacts of airflow pressure angle, and velocity ratio on the relative frequency change (RFC) of the nanoclay-reinforced concrete shell structures under airflow pressure considering $K_w^* = 1$, $C_d^* = 1$, $P^*/P_0 = 1$, $L/R = 10$, $R/h = 10$, $NCWF = 2[\%]$, clamped–clamped boundary conditions and Pattern X.

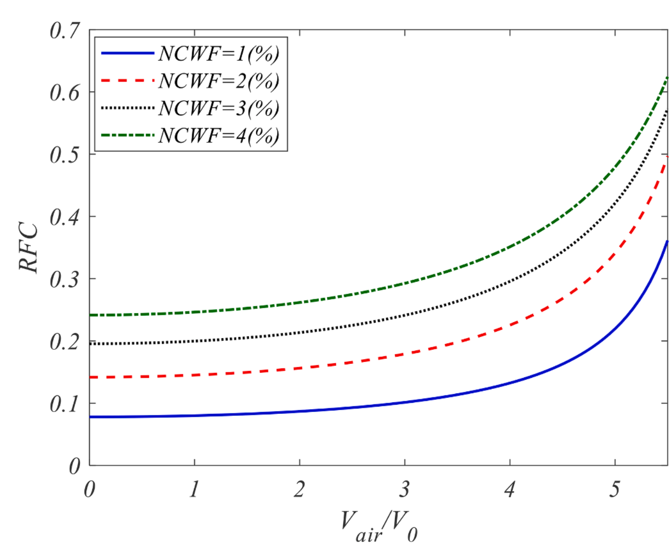

Fig. 4. The impacts of airflow pressure velocity ratio and nanoclay weight fraction (NCWF) on the RFC of the nanoclay-reinforced concrete shell structures under airflow pressure considering $K_w^* = 1$, $C_d^* = 1$, $P^*/P_0 = 1$, $L/R = 10$, $R/h = 10$, $\theta_{air} = \pi/4$, clamped–clamped boundary conditions and Pattern X.

Overall, the table highlights that the present model closely follows the trends of the experimental dataset, with minor deviations. These variations may arise from differences in modeling assumptions, material properties, or computational methods, yet the results demonstrate good agreement, validating the proposed approach for frequency prediction in cylindrical shells.

4.2. Convergence study

The convergence of non-dimensional frequencies on boundary spring stiffness with different boundary conditions is presented in Table 3. As mentioned earlier, the sets of linear springs with stiffnesses for various boundary conditions, such as simply supported and clamped, can be obtained by appropriately setting the values of the spring stiffness. Their value is dependent on the convergence study of the results that are presented in this part. For clamped–clamped boundary conditions, $\mathscr{F}_{\mathscr{U}}=\mathscr{F}_{\mathscr{V}}=\mathscr{F}_{\mathscr{W}} = \mathscr{F}$; for simply-supported boundary conditions, $\mathscr{F}_{\mathscr{U}}=0$, and $\mathscr{F}_{\mathscr{V}} = \mathscr{F}_{\mathscr{W}} = \mathscr{F}$. As can be seen in Table 3, selecting $\mathscr{F} = 10^{15}$ is appropriate for reaching the convergence result of the presented study.

4.3. Parametric results

It should be noted that relative frequency change (RFC) is presented to show the sensitivity of the current concrete shell structure to the nanoclay reinforcement. In other word, RFC is computed using the following formulation:

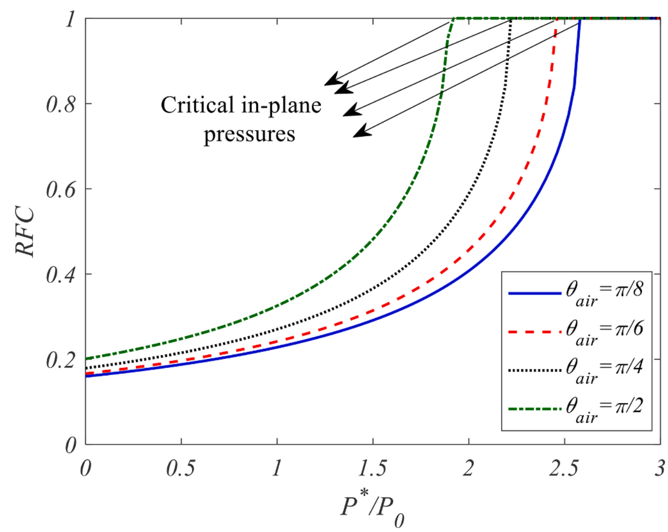

Fig. 6. The impacts of in-plane pressure ratio, and airflow pressure angle on the RFC of the nanoclay-reinforced concrete shell structures under airflow pressure considering $K_w^* = 1$, $C_d^* = 1$, $L/R = 10$, $R/h = 10$, $V_{air}/V_0 = 3$, $NCWF = 2[\%]$, clamped–clamped boundary conditions, and Pattern X.

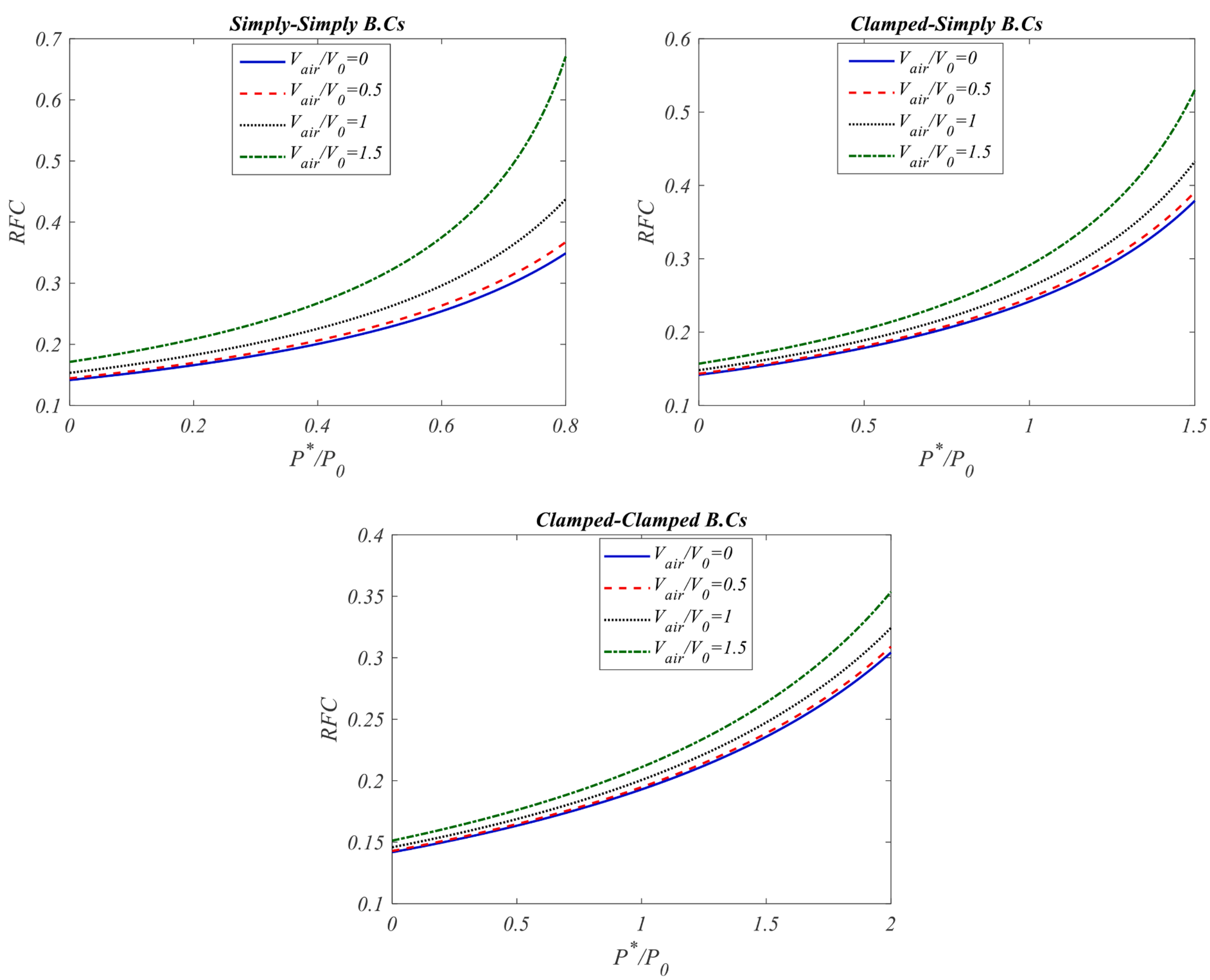

Fig. 5. The impacts of in-plane pressure ratio, airflow pressure velocity ratio, and boundary conditions on the RFC of the nanoclay-reinforced concrete shell structures under airflow pressure considering $K_w^* = 1$, $C_d^* = 1$, $L/R = 10$, $R/h = 10$, $V_{air}/V_0 = 3$, $\theta_{air} = \pi/4$, $NCWF = 2[\%]$, and Pattern X.

$$RFC = (\omega_1 - \omega_2)/\omega_1. \quad (45)$$

In Eq. (58), ω_1 and ω_2 show the resonance frequency value of the current structure considering and without considering nanoclay as the reinforcement, respectively.

Fig. 3 illustrates the influence of airflow pressure angle and velocity ratio on the RFC of nanoclay-reinforced concrete shell structures subjected to airflow pressure. The RFC, represented on the vertical axis, indicates the variation in natural frequency due to the applied aerodynamic conditions. The horizontal axis denotes the normalized velocity ratio, V_{air}/V_0 , where V_0 is the reference velocity ($100m/s$). The curves correspond to different airflow pressure angles: $\pi/8, \pi/6, \pi/4$, and $\pi/2$, with the critical velocity for each condition marked. It is observed that for lower-pressure angles (e.g., $\theta_{air} = \pi/8$), the structure demonstrates greater stability, as the RFC increases more gradually with the velocity ratio. Conversely, as the pressure angle increases (e.g., $\theta_{air} = \pi/2$), the RFC grows sharply, indicating earlier resonance and reduced stability. The critical V_{air}/V_0 values, where the transition from stability in response (S.I.R) to instability in response (IS.I.R) occurs, are clearly annotated. This signifies the onset of resonance frequency conditions, beyond which the structural integrity degrades. The figure emphasizes the interplay between aerodynamic pressure distribution and structural dynamics, vital for optimizing stability under varying operational conditions.

Fig. 4 demonstrates the effects of airflow pressure velocity ratio and nanoclay weight fraction (NCWF) on the RFC of nanoclay-reinforced concrete shell structures under aerodynamic pressure. The RFC, plotted on the vertical axis, quantifies the natural frequency variation, while the horizontal axis represents the normalized velocity ratio. The figure includes curves for four NCWF levels: 1 %, 2 %, 3 %, and 4 %. It is evident that as the NCWF increases, the RFC rises for a given V_{air}/V_0, highlighting the beneficial role of nanoclay in enhancing structural stiffness. At NCWF = 1 % (blue curve), the RFC growth is minimal across the velocity range, signifying lower structural sensitivity to aerodynamic pressure. In contrast, the NCWF = 4 % curve (green) shows a pronounced RFC increase, indicating stronger interaction between the nanoclay-reinforced material and airflow dynamics. The overall trend reveals that higher NCWF values improve the resonance frequency response, delaying the onset of instability (IS.I.R) as V_{air}/V_0 increases. This underscores the importance of nanoclay reinforcement in tailoring

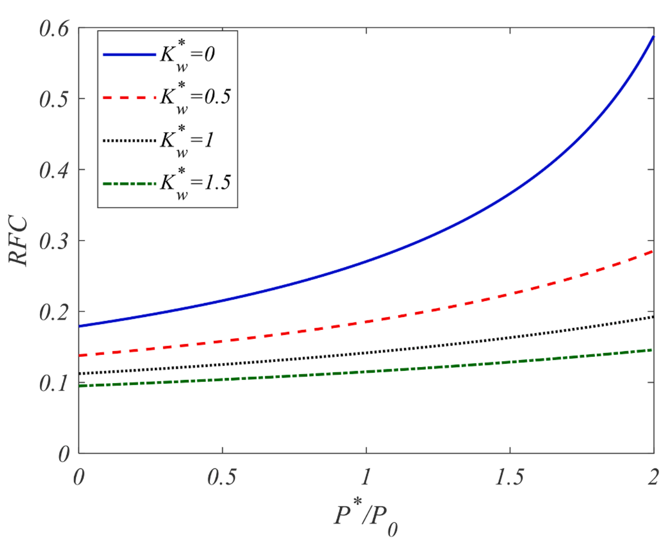

Fig. 7. The impacts of in-plane pressure ratio, and dimensionless Winkler parameter on the RFC of the nanoclay-reinforced concrete shell structures under airflow pressure considering $C_d^* = 1, L/R = 10, R/h = 10, V_{air}/V_0 = 3$, $\theta_{air} = \pi/4$, $NCWF = 2[\%]$, clamped–clamped boundary conditions and Pattern X.

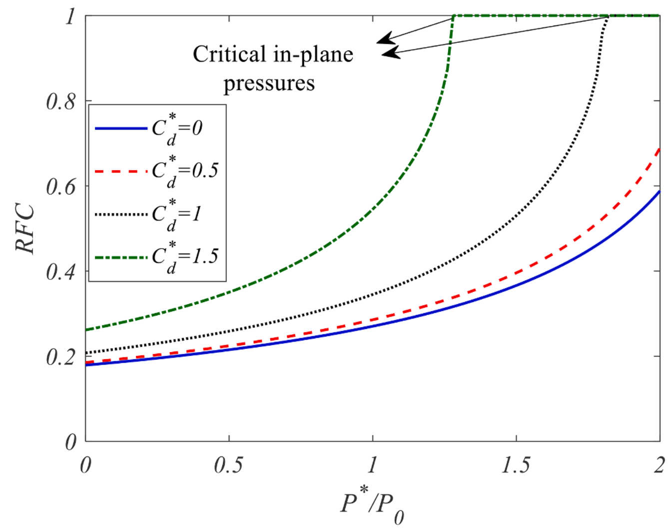

Fig. 8. The impacts of in-plane pressure ratio, and dimensionless damping parameter on the RFC of the nanoclay-reinforced concrete shell structures under airflow pressure considering $K_w^* = 1, L/R = 10, R/h = 10, V_{air}/V_0 = 3$, $\theta_{air} = \pi/4$, $NCWF = 2[\%]$, clamped–clamped boundary conditions and Pattern X.

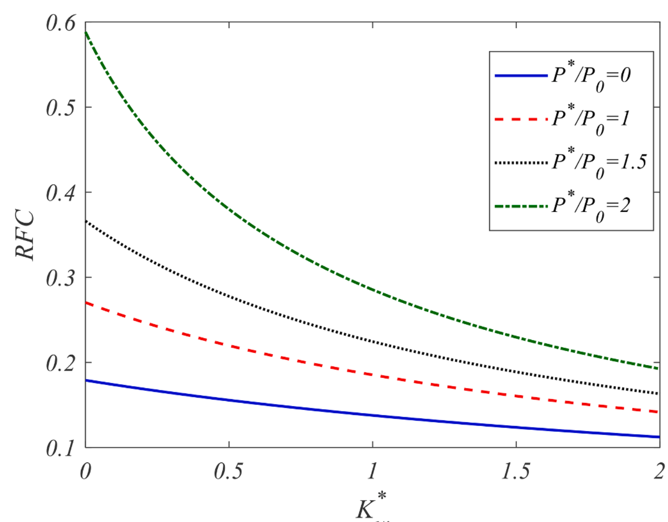

Fig. 9. The impacts of dimensionless Winkler parameter and in-plane pressure ratio on the RFC of the nanoclay-reinforced concrete shell structures under airflow pressure considering $C_d^* = 1, L/R = 10, R/h = 10, V_{air}/V_0 = 3, \theta_{air} = \pi/4$, $NCWF = 2[\%]$, clamped–clamped boundary conditions and Pattern X.

the aerodynamic and structural performance of concrete shells, particularly for applications involving high-pressure aerodynamic environments.

Fig. 5 explores the combined effects of in-plane pressure ratio, airflow pressure velocity ratio, and boundary conditions on the RFC of nanoclay-reinforced concrete shell structures. The figure consists of three subplots, corresponding to different boundary conditions: simply-simply (top left), clamped-simply (top right), and clamped–clamped (bottom). Each subplot illustrates the RFC against the normalized in-plane pressure ratio for three values of V_{air}/V_0 : 0.5, 1, and 1.5. Across all boundary conditions, the RFC increases with both P^*/P_0 and V_{air}/V_0. The clamped–clamped case (bottom) shows the least sensitivity to changes in P^*/P_0 and V_{air}/V_0 , indicating higher structural stability. In contrast, the simply-simply case (top left) exhibits a more pronounced RFC increase, reflecting greater susceptibility to aerodynamic and in-plane pressure effects. The clamped-simply case (top right) demonstrates intermediate behavior, where clamping enhances stability compared to the simply-supported configuration but is less effective than full clamping. This figure underscores the critical role of boundary conditions in modulating resonance behavior and stability under combined aerodynamic and in-plane pressure conditions, offering insights into optimizing structural designs for enhanced performance.

Fig. 6 illustrates the relationship between the RFC and the normalized in-plane pressure ratio for nanoclay-reinforced concrete shell structures subjected to airflow pressure. Different curves correspond to various airflow pressure angles ranging from π/8 to π/2. As shown, the RFC increases nonlinearly with increasing in-plane pressure ratios for all angles. The results highlight that higher airflow angles lead to earlier critical pressure points, where the RFC approaches instability. Specifically, the $\theta_{air} = \pi/2$ case (green dash-dot line) reaches critical resonance at a lower pressure ratio compared to the $\theta_{air} = \pi/8$ case (solid blue line), indicating increased susceptibility to instability (IS.I. R) at higher angles. The marked arrows identify critical in-plane pressures, where structural stability transitions from stability in response (S.I. R) to instability in response. These findings emphasize the role of both in-plane pressure and airflow angles in governing resonance behavior and structural stability. This analysis is crucial for predicting failure thresholds in shell structures under dynamic loads, aiding in their design and safety assessment.

Fig. 7 illustrates the effect of the in-plane pressure ratio and the dimensionless Winkler parameter on the RFC of nanoclay-reinforced concrete shell structures subjected to airflow pressure. Four curves represent different values of the Winkler parameter which model the stiffness of the elastic foundation. The results indicate that higher Winkler parameter values reduce the RFC, implying improved structural stability due to increased foundation stiffness. Specifically, the blue curve ($K_w^* = 0$) shows the highest sensitivity to pressure variations, leading to greater RFC and potential instability. Conversely, the green dash-dot curve ($K_w^* = 1.5$) exhibits minimal RFC, reflecting enhanced stability. This behavior highlights the stabilizing effect of the elastic foundation, which mitigates resonance frequency shifts under pressure. The findings underscore the importance of incorporating nanoclay reinforcement and foundation stiffness adjustments in designing stable shell structures, particularly in environments with dynamic pressure conditions.

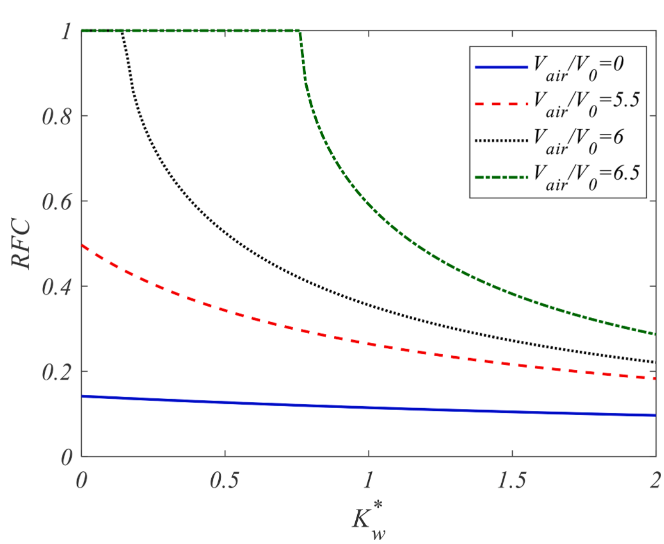

Fig. 10. The impacts of dimensionless Winkler parameter and airflow pressure velocity ratio on the RFC of the nanoclay-reinforced concrete shell structures under airflow pressure considering $C_d^* = 1$, $P^*/P_0 = 1$, $L/R = 10$, $R/h = 10$, $\theta_{air} = \pi/4$, $NCWF = 2[\%]$, clamped–clamped boundary conditions and Pattern X.

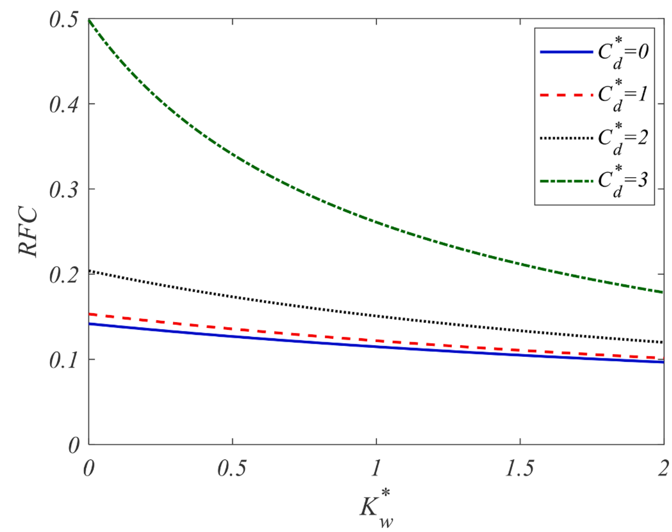

Fig. 11. The impacts of the dimensionless Winkler parameter and dimensionless damping parameter on the RFC of the nanoclay-reinforced concrete shell structures under airflow pressure considering $P^*/P_0 = 1$, $L/R = 10$, $R/h = 10$, $V_{air}/V_0 = 3$, $\theta_{air} = \pi/4$, $NCWF = 2[\%]$, clamped–clamped boundary conditions and Pattern X.

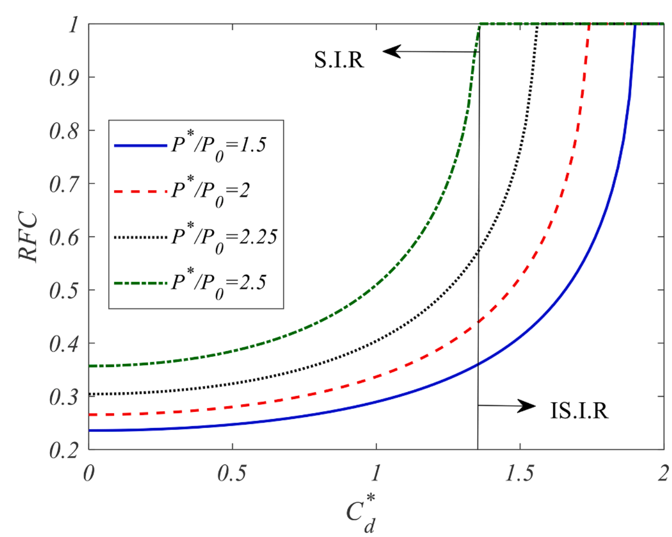

Fig. 12. The impacts of dimensionless Winkler parameter and dimensionless in-plan pressure on the RFC of the nanoclay-reinforced concrete shell structures under airflow pressure considering $K_w^* = 1$, $L/R = 10$, $R/h = 10$, $V_{air}/V_0 = 3$, $\theta_{air} = \pi/4$, $NCWF = 2[\%]$, clamped–clamped boundary conditions and Pattern X.

Fig. 8 investigates the effect of the in-plane pressure ratio and the dimensionless damping parameter on the RFC of nanoclay-reinforced concrete shell structures under airflow pressure. As the damping parameter increases, the RFC grows more rapidly with increasing pressure, indicating reduced stability. Specifically, the green dash-dot curve ($C_d^* = 1.5$) reaches critical resonance conditions at a lower pressure ratio, suggesting earlier instability compared to the blue curve ($C_d^* = 0$), which maintains stability over a wider pressure range. Arrows mark the critical in-plane pressures, where resonance frequency shifts significantly, highlighting the onset of instability. The results emphasize that higher damping reduces the system's ability to dissipate energy, making it more susceptible to dynamic instability. This analysis underscores the importance of optimizing damping characteristics in conjunction with nanoclay reinforcement to enhance the stability of concrete shell structures under variable pressure conditions.

Fig. 9 illustrates the relationship between the relative frequency change of nanoclay-reinforced concrete shell structures and the dimensionless Winkler parameter under varying in-plane pressure ratios in the presence of airflow pressure. The figure indicates that for all cases, the RFC decreases as K_w^* increases, signifying reduced sensitivity of the structure's resonance frequency to reinforcement as the foundation stiffness increases. At lower K_w^*, RFC values are higher, suggesting greater structural sensitivity. Additionally, higher in-plane pressure ratios result in elevated RFC values across the entire range of K_w^*. This trend demonstrates that greater in-plane pressures amplify the resonance frequency sensitivity to nanoclay reinforcement, possibly pushing the structure closer to instability. Notably, when$P^*/P_0 = 0$, the structure exhibits the least sensitivity (lowest RFC), implying higher stability. Conversely, P^*/P_0=2 corresponds to the highest RFC values, indicating higher susceptibility to instability under critical conditions. This highlights the influence of in-plane pressure and foundation stiffness on the dynamic behavior of reinforced concrete shells.

Fig. 10 explores the relationship between the relative frequency change of nanoclay-reinforced concrete shell structures and the dimensionless Winkler parameter, under varying airflow pressure velocity ratios. The RFC consistently decreases as K_w^* increases for all velocity ratios, indicating that increasing foundation stiffness mitigates resonance frequency sensitivity. When K_w^* is low, RFC values are significantly higher, reflecting greater sensitivity to nanoclay reinforcement under low foundation stiffness conditions. As the airflow pressure velocity ratio increases, the RFC values across all K_w^* levels become progressively larger. Specifically, when$V_{air}/V_0 = 6.5$, the RFC reaches its highest values, signifying heightened sensitivity and potential for instability. Conversely, at$V_{air}/V_0 = 0$, RFC values are minimal, representing the most stable conditions. The sharp increase in RFC at higher airflow velocities highlights the destabilizing influence of aerodynamic forces, especially when combined with low foundation stiffness. This underscores the importance of optimizing both material reinforcement and pressure conditions to ensure stability in nanoclay-reinforced concrete shell structures.

Fig. 11 presents the effects of the dimensionless Winkler parameter and dimensionless damping parameter on the relative frequency change of nanoclay-reinforced concrete shell structures under airflow pressure. The RFC values decrease as K_w^* increases for all C_d^* cases, indicating that

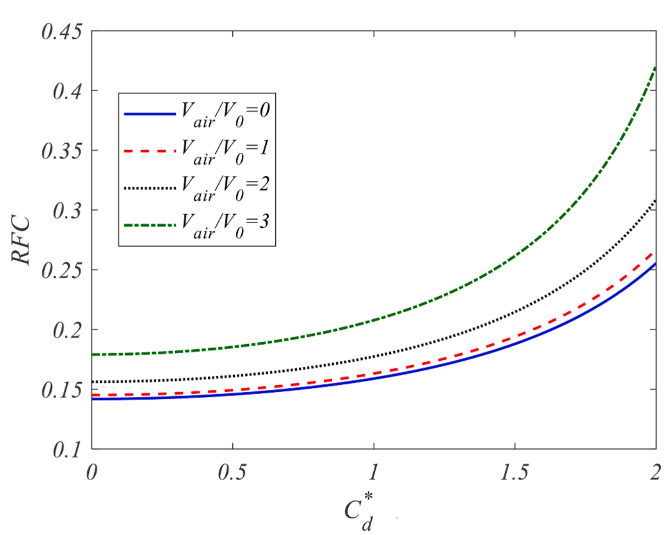

Fig. 13. The impacts of dimensionless damping parameter and airflow pressure velocity ratio on the RFC of the nanoclay-reinforced concrete shell structures under airflow pressure considering $K_w^* = 1$, $P^*/P_0 = 1$, $L/R = 10$, $R/h = 10$, $\theta_{air} = \pi/4$, $NCWF = 2[\%]$, clamped–clamped boundary conditions and Pattern X.

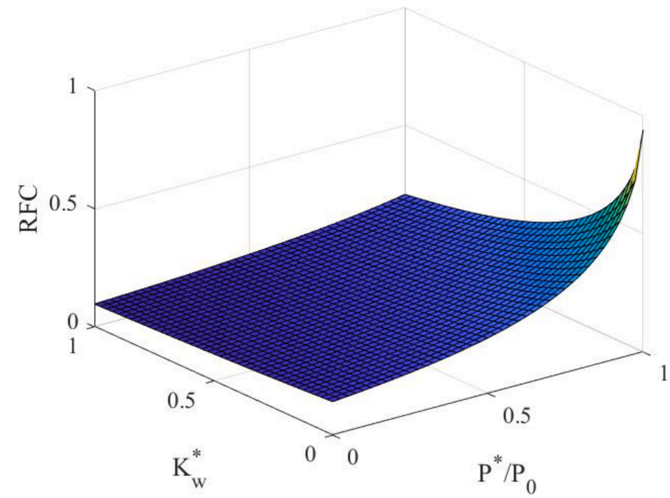

Fig. 14. The impacts of dimensionless Winkler parameter and in-plane pressure ratio on the RFC of the nanoclay-reinforced concrete shell structures under airflow pressure considering $C_d^* = 1$, $L/R = 10$, $R/h = 10$, $V_{air}/V_0 = 3$, $\theta_{air} = \pi/4$, $NCWF = 2[\%]$, clamped–clamped boundary conditions and Pattern X.

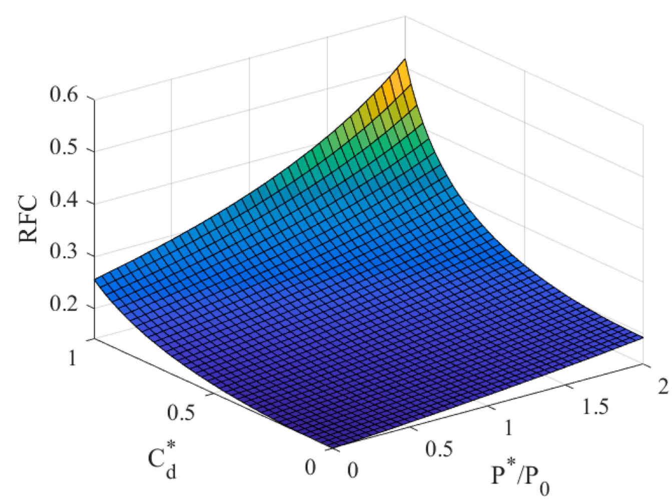

Fig. 15. The impacts of dimensionless damping parameter and in-plane pressure ratio on the RFC of the nanoclay-reinforced concrete shell structures under airflow pressure considering $K_w^* = 1$, $L/R = 10$, $R/h = 10$, $V_{air}/V_0 = 3$, $\theta_{air} = \pi/4$, $NCWF = 2[\%]$, clamped–clamped boundary conditions and Pattern X.

increased foundation stiffness reduces sensitivity to nanoclay reinforcement. At higher damping parameters, the RFC values across the range of K_w^* are elevated, signifying that increased damping enhances the resonance frequency sensitivity of the structure. When $C_d^* = 0$, the lowest RFC values are observed, suggesting maximum stability. As C_d^* increases to 3, the RFC reaches its peak, indicating heightened structural sensitivity and potential instability. This trend underscores the destabilizing effect of increased damping, which amplifies the dynamic response of the system under airflow pressure. The figure highlights the combined roles of foundation stiffness and damping in influencing the stability and resonance behavior of nanoclay-reinforced concrete shell structures. Optimal control of these parameters is critical for achieving desired structural performance and minimizing the risk of instability.

Fig. 12 illustrates the relationship between the relative frequency change and the dimensionless Winkler parameter for nanoclay-reinforced concrete shell structures subjected to varying airflow pressures. The RFC increases with C_d^* for all pressure ratios, signifying enhanced sensitivity of the structure's resonance frequency as the

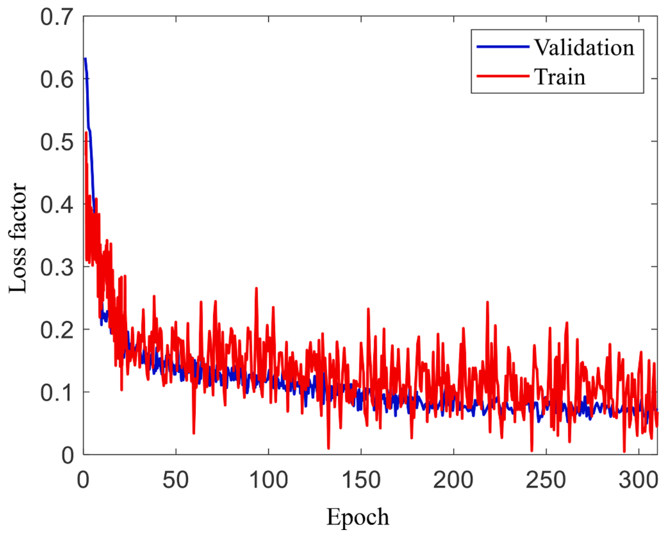

Fig. 16. Loss factor against epoch for training and validation dataset.

Winkler parameter increases. At lower C_d^*, the curves exhibit relatively gradual changes, indicating stability in response (S.I.R). However, as C_d^* exceeds a critical threshold ($C_d^* > 1.5$), marked by a vertical boundary, a rapid escalation in RFC is observed, transitioning the structure into instability in response. Higher pressure ratios amplify the sensitivity, as evidenced by the steepness of the curves. For instance, the green curve ($P^*/P_0 = 2.5$) shows the most pronounced response, indicating a greater likelihood of resonance-induced instability under high-pressure conditions. This behavior demonstrates that both the reinforcement properties and applied pressure significantly affect the structural dynamics. Overall, the figure emphasizes the critical role of nanoclay reinforcement in modulating stability and underscores the importance of controlling C_d^* to mitigate instability risks in concrete shell structures.

Fig. 13 depicts the effect of the dimensionless damping parameter and airflow pressure velocity ratio on the RFC for nanoclay-reinforced concrete shell structures under airflow pressure. As C_d^* increases, the RFC demonstrates a consistent upward trend across all velocity ratios, highlighting the enhanced sensitivity of the resonance frequency to damping. At lower values of C_d^*, the changes in RFC are minimal, indicating a stable structural response. However, as C_d^* grows, the RFC increases more significantly, especially for higher velocity ratios ($V_{air}/V_0 = 3$), as observed in the steepest green curve. The figure underscores that the effect of airflow pressure velocity ratio becomes more pronounced at higher C_d^*, suggesting that increased airflow amplifies the impact of damping on the structural dynamics. Comparatively, the lowest velocity ratio results in the least RFC, indicating reduced sensitivity in the absence of airflow pressure. This analysis demonstrates the critical interplay between damping and airflow velocity in influencing the stability and resonance behavior of reinforced concrete shell structures under dynamic conditions.

Table 4
The influence of $RMSE_{Train}$ on correcting the results of the mentioned algorithm for various P^*/P_0 considering $K_w^* = 1, C_d^* = 1, L/R = 10, R/h = 10, V_{air}/V_0 = 3, \theta_{air} = \pi/4$, $NCWF = 2[\%]$, clamped–clamped boundary conditions and Pattern X.

P^*/P_0	MS	Predicted $RMSE_{Train}$ = 0.3152	$RMSE_{Train}$ = 0.3593	$RMSE_{Train}$ = 0.3891
0	1.16287	0.89806	1.10766	1.16434
0.15	0.97762	0.80106	0.89637	0.97761
0.3	0.65844	0.44981	0.57359	0.65917
0.45	0.42185	0.35039	0.3928	0.42325
0.6	0.2299	0.14693	0.22005	0.22979

Table 5
The influence of R^2 on correcting results of the mentioned algorithm for various $NCWF(\%)$ considering $K_w^* = 1$, $C_d^* = 1$, $P^*/P_0 = 1$, $L/R = 10$, $R/h = 10$, $V_{air}/V_0 = 3$, $\theta_{air} = \pi/4$, clamped–clamped boundary conditions, and Pattern X.

$NCWF(\%)$	MS	Predicted $R^2 = 0.9121$	$R^2 = 0.9512$	$R^2 = 0.9912$
0	0.57139	0.42302	0.53535	0.5727
1	0.82138	0.57359	0.70371	0.82045
1.5	0.89503	0.67301	0.83727	0.89493
2	1.30572	0.94098	1.11295	1.30664
2.5	1.56686	1.19855	1.48866	1.56802

Fig. 14 shows the effect of the dimensionless Winkler parameter and the in-plane pressure ratio on the relative frequency change of nanoclay-reinforced concrete shell structures. The RFC increases with both K_w^* and P^*/P_0, indicating that greater reinforcement stiffness and higher in-plane pressure amplify the resonance frequency response of the structure. For small values of K_w^* and P^*/P_0, the RFC remains relatively low and stable, reflecting a limited sensitivity to dynamic effects. However, as these parameters increase, the RFC exhibits a sharp rise, particularly at higher P^*/P_0, demonstrating enhanced instability in response. This behavior underscores the influence of both reinforcement stiffness and in-plane pressure on the stability and dynamic characteristics of reinforced shell structures under airflow conditions.

Fig. 15 examines the impact of the dimensionless damping parameter and in-plane pressure ratio on the RFC of nanoclay-reinforced concrete shell structures. The RFC shows a nonlinear growth as both C_d^* and P^*/P_0 increase. At lower values of these parameters, the RFC remains minimal, indicating stability. However, as P^*/P_0 and C_d^* rise, the RFC demonstrates a steeper increase, reflecting an enhanced sensitivity to damping effects under higher in-plane pressures. The interaction between damping and pressure suggests that controlling C_d^* is essential for mitigating dynamic instability in reinforced shell structures subjected to airflow-induced stresses.

4.4. Results of presented DNN-fuzzy algorithm

As mentioned in the previous section, the results of the mathematics simulation are used as the input values of the presented DNN-fuzzy algorithm. It should be noted that 4820 datasets are collected for collecting the results. Fig. 16 illustrates the loss factor plotted against the number of epochs for both training and validation datasets during the training process of a machine learning model. The loss factor represents the error or deviation between the predicted and actual values, serving as an indicator of the model's performance. The x-axis denotes the number of epochs, which refers to the number of iterations through the entire training dataset, while the y-axis represents the loss factor. Initially, both the training and validation loss factors are relatively high, indicating a significant error in the model's predictions. However, as the number of epochs increases, the loss factors for both datasets exhibit a general downward trend, suggesting that the model improves its predictions by learning from the data. The rapid decrease in loss during the initial epochs demonstrates the effectiveness of the optimization algorithm in minimizing the error. The training loss fluctuates more than the validation loss due to the model's iterative adjustment of weights based on the training dataset. The validation loss remains consistently lower and smoother, indicating the model's ability to generalize well without overfitting. By the 300th epoch, the loss factors stabilize at lower values for both datasets, reflecting convergence and improved model performance. This figure highlights the model's successful training and validation process.

Table 4 presents the influence of $RMSE_{Train}$ on the accuracy of predicted results for various values of the in-plane pressure ratio. The first column lists P^*/P_0, which quantifies the ratio of applied pressure (P^*) to a reference pressure (P_0). The second column (MS) represents the actual measured values of a property affected by the pressure ratio. The remaining columns show the predicted results for three different levels of $RMSE_{Train}$: 0.3152, 0.3593, and 0.3891. As P^*/P_0 increases, the MS values decrease, indicating a nonlinear relationship between the pressure ratio and the measured property. For each $RMSE_{Train}$, the predicted values are presented to evaluate the model's accuracy. Lower values of $RMSE_{Train}$ correspond to predictions that more closely match the measured data (MS), suggesting improved performance of the algorithm. For instance, when $RMSE_{Train} = 0.3152$, the predicted values align more closely with the MS values across all P^*/P_0 levels compared to higher RMSE values. This table demonstrates how minimizing $RMSE_{Train}$ during the training phase enhances the model's ability to predict outcomes accurately, emphasizing the importance of robust training processes for reliable predictions in applications involving structural pressure ratios.

Table 5 evaluates the influence of R^2 on the accuracy of predicted results for various nanoclay weight fractions, measured in %). The first column lists the *NCWF* values, indicating the proportion of nanoclay in the material. The second column (MS) contains the measured (true) values of a property affected by *NCWF*. The subsequent columns present the predicted results for three levels of R^2: 0.9121, 0.9512, and 0.9912. As *NCWF* increases, the MS values also increase, indicating that the property under consideration positively correlates with nanoclay content. Predictions made by the algorithm improve as R^2 increases. When $R^2 = 0.9912$, the predicted values align closely with the MS values across all *NCWF* levels, demonstrating the highest predictive accuracy. Conversely, when $R^2 = 0.9121$, the predictions show a larger deviation from the MS values, particularly at higher *NCWF* percentages. This table highlights the importance of achieving high R^2 values for accurate modeling and prediction. As R^2 approaches 1, the model captures the variance in the data more effectively, leading to predictions that are more reliable and closely aligned with the actual measurements.

5. Conclusion

This study measured the resonance frequency and relative frequency changes in concrete cylindrical shells reinforced with nanoclay and resting on viscoelastic foundations under combined in-plane and airflow pressures. Through advanced mathematical modeling, the natural frequencies of the system were determined, considering the influence of nanoclay reinforcement and the viscoelastic behavior of the foundation, represented by a Kelvin-Voigt framework. The measurement of structural response was conducted using parameterized simulations, providing detailed insights into the effects of varying nanoclay content and in-plane pressures on frequency characteristics. The accuracy and reliability of the mathematical model were validated using experimental datasets from the literature and a deep neural network integrated with a fuzzy algorithm. This computational approach ensured robust verification of the analytical results. The measurements demonstrated that nanoclay reinforcement significantly improved the stiffness and stability of the shells, resulting in higher natural frequencies. Furthermore, the interaction between in-plane pressure and airflow pressure was shown to induce mechanical effects that were captured accurately through the proposed model. This research provides a measurement-centric framework for evaluating the dynamic behavior of reinforced cylindrical shells. The findings highlight the importance of nanoclay as a reinforcing material in enhancing structural performance, particularly under complex pressure conditions. The integration of computational intelligence methods, such as the DNN-fuzzy algorithm, with traditional measurement techniques ensures high precision and reliability, setting a benchmark for similar studies in structural dynamics. By combining accurate measurement methods with advanced modeling and verification techniques, this study contributes to the broader field of structural optimization in aeronautical and civil engineering applications. These results underscore the critical role of precise frequency measurement in understanding the interplay between material enhancements, pressures, and foundation properties, paving the way for future advancements in the design and analysis of reinforced structures.

CRediT authorship contribution statement

Zhonghong Li: Writing – review & editing, Visualization, Validation, Software, Resources, Investigation. **Yang Bing:** Writing – review & editing, Writing – original draft, Visualization, Validation, Supervision, Software, Resources, Formal analysis, Data curation, Conceptualization. **Suming Chen:** Writing – review & editing, Visualization, Validation, Software, Resources, Investigation. **Mohammed El-Meligy:** Writing – review & editing, Validation, Software, Resources, Investigation. **Mubariz Garayev:** Writing – review & editing, Software, Resources, Investigation.

Declaration of competing interest

The authors declare that they have no known competing financial interests or personal relationships that could have appeared to influence the work reported in this paper.

Acknowledgements

The authors extend their appreciation to King Saud University for funding this work through Researchers Supporting Project number (RSPD2024R1056), King Saud University, Riyadh, Saudi Arabia.

Data availability

Data will be made available on request.

References

[1] A. Kausar, I. Ahmad, O. Aldaghri, K.H. Ibnaouf, M. Eisa, Nanoclay-reinforced nanocomposite nanofibers—Fundamentals and state-of-the-art developments, *Minerals* 13 (6) (2023) 817.

[2] L.O. Ejeta, Nanoclay/organic filler-reinforced polymeric hybrid composites as promising materials for building, automotive, and construction applications-a state-of-the-art review, *Compos. Interfaces* 30 (12) (2023) 1363–1386.

[3] A.A. Aghdam, M.H. Niaki, M. Sakkaki, Effect of basalt fibers on fracture properties of nanoclay reinforced polymer concrete after exposure to elevated temperatures, *Journal of Building Engineering* 76 (2023) 107329.

[4] E. Dias, et al., Review on synthetic/natural fibers polymer composite filled with nanoclay and their mechanical performance, *Mater. Today Proc.* 77 (2023) 916–925.

[5] P. Azhagiri, N. Senthilkumar, K. Palanikumar, B. Deepanraj, Mechanical properties evaluation on hybrid AA6026 composites added with nanoclay and carbon fibers, *Carbon Letters* 33 (3) (2023) 833–846.

[6] P.H. Puttaswamygowda, S. Sharma, A.K. Ullal, M. Shettar, Synergistic Enhancement of the Mechanical Properties of Epoxy-Based Coir Fiber Composites through Alkaline Treatment and Nanoclay Reinforcement, *Journal of Composites Science* 8 (2) (2024) 66.

[7] D. Shelly, et al., Exploring the Impact of Nanoclay on Epoxy Nanocomposites: A Comprehensive Review, *Journal of Composites Science* 8 (12) (2024) 506.

[8] R.K. Ramakrishnan, N.S. Sumitha, "Nanoclay-reinforced polymers," in *Nanoclay-Based Sustainable Materials*, Elsevier (2024) 91–114.

[9] M.N. Uddin, et al., Research and applications of nanoclays: A review, *SPE Polym.* 5 (4) (2024) 507–535.

[10] X. Liang, Q. Li, Y. Ren, W. Xie, A. Tang, H. Yang, Nanoclay Reinforced Polymer Composite Dielectrics for Ultra-Balanced Electrostatic Energy Storage, *Adv. Funct. Mater.* 34 (48) (2024) 2408719.

[11] A. Kausar, "Nanoclay Reinforced Thermoplastic Polymeric Nanocomposite Membranes—State-of-the-Art and Progresses," *Polymer-Plastics Technology and Materials*, pp. 1–23, 2024.

[12] H. Ibrahim, et al., Design and validation of a multi-electrode embedded capacitive sensor to monitor the electromagnetic properties in reinforced concrete structures, *Measurement* (2024) 115057.

[13] S. Zhang, L. Liao, J. Zhou, K. Tong, R. Xia, H. Zhang, Anti-electromagnetic interference encapsulation method for resonance-enhanced magnetoelastic sensors inside prestressed concrete structures, *Measurement* 238 (2024) 115368.

[14] C. Zhang, J. Chen, W. Li, F. Xiong, X. Deng, Optimization scheme of water irrigation and electric heating method for multi-crack detection in wading-concrete structures, *Measurement* 228 (2024) 114353.

[15] C. Xue, D. Kong, B. Li, C. Xu, Dynamic matching error of stress sensors in concrete structures, *Measurement* 224 (2024) 113893.

[16] Z. Niu, et al., Bayesian approach for uncertainty quantification in elastic wave tomography of concrete structures, *Measurement* 243 (2025) 116327.

[17] Y. Li, et al., Influence of inerter on torsional natural frequency of single-layer vibration system, *Measurement* 241 (2025) 115678.

[18] G. Sha, W. Xiao, H. Zuo, M. Cao, M. Radzieński, W. Ostachowicz, Global-local damage localization and imaging in beam structures using laser-measured natural frequencies and guided wavefields, *Measurement* (2024) 115061.

[19] D. Zhang, et al., Real-time tension estimation in the spinning process based on the natural frequencies extraction of the Polyester Filament Yarn, *Measurement* 188 (2022) 110514.

[20] G. Sha, R. Soman, M. Radzieński, M. Cao, W. Ostachowicz, H. Zuo, A two-step method for additional mass identification in beam structures by measurements of natural frequencies and guided waves, *Measurement* 186 (2021) 110049.

[21] Y. Cheng, et al., Computer vision-based non-contact structural vibration measurement: Methods, challenges and opportunities, *Measurement* (2024) 116426.

[22] T.Q. Quan, V.M. Anh, N.D. Duc, Natural frequency analysis of sandwich plate with auxetic honeycomb core and CNTRC face sheets using analytical approach and artificial neural network, *Aerosp. Sci. Technol.* 144 (2024) 108806.

[23] O. Outassafte, A. Adri, Y.E. Khouddar, I.E. Hantati, S. Rifai, R. Benamar, Crack identification in circular arches through natural frequency variations and the firefly hybrid algorithm, *Mech. Adv. Mater. Struct.* 31 (22) (2024) 5701–5715.

[24] L. Zhang, W. Liao, J. Fan, A novel surrogate-based crack identification method for cantilever beam based on the change of natural frequencies, *Comput. Struct.* 292 (2024) 107243.

[25] L.C. Luan, Formula for the Dependence of the Fundamental Natural Frequency of a Regular Truss on the Number of Panels, in: Presented at the 2024 6th International Youth Conference on Radio Electronics, Electrical and Power Engineering (REEPE), 2024, pp. 1–5.

[26] T. Guo, H. Song, S. Sha, C. Li, M. Xu, Highly sensitive fiber bragg grating accelerometer with low resonant frequency, *Opt. Fiber Technol.* 87 (2024) 103919.

[27] S. Beheshtian, S.K. Roodbari, H. Ghorbani, M. Azodinia, M. Mudabbir, A. R. Varkonyi-Koczy, Advanced Machine Learning Methods for Accurate Prediction of Loss Circulation in Drilling Well Log, in: Presented at the 2024 IEEE 11th International Conference on Computational Cybernetics and Cyber-Medical Systems (ICCC), 2024, pp. 000031–000036.

[28] H. Ghorbani *et al.*, "ENHANCING DIABETES MELLITUS PREDICTION AND SURVEILLANCE: A HYBRID MACHINE LEARNING APPROACH".

[29] K.K. Gupta, L. Roy, S. Dey, Hybrid machine-learning-assisted stochastic nano-indentation behaviour of twisted bilayer graphene, *J. Phys. Chem. Solid* 167 (2022) 110711.

[30] S.V. Alavi Nezhad Khalil Abad, et al., Determination of the rate of penetration by robust machine learning algorithms based on drilling parameters, *ACS Omega* 8 (49) (2023) 46390–46398.

[31] H. Ghorbani, et al., Application of a new hybrid machine learning (fuzzy-pso) for detection of breast's tumor," presented at the 2023 IEEE 21st World Symposium on Applied Machine Intelligence and Informatics (SAMI), IEEE 2023 (2023) 000147–000154.

[32] Y. Wang, Y. Cao, X. Qu, M. Wang, Y. Wang, C. Zhang, A review of the application of machine learning techniques in thermal error compensation for CNC machine tools, *Measurement* (2024) 116341.

[33] X. Zhang, T. Hu, Y. Wu, L. Yang, J. Wang, J. He, ACDE2LM: Autocorrelation-constrained dynamic ensemble extreme learning machine for real-time fault diagnostics of bearings, *Measurement* (2024) 116608.

[34] M.H. Bagherian, Y.H. Tehrani, S.M. Atarodi, Enhancing LoRaWAN localization efficiency: Leveraging machine learning and optimized parameter tuning for a 60% improvement, *Measurement* 242 (2025) 116064.

[35] P. Liang, F. Duan, J. Wang, H. Zhou, Localization method for rock acoustic emission sources based on single sensor data and SVR-GBR machine learning models, *Measurement* (2024) 116566.

[36] A. Daas, B. Sari, J. Jia, G. Rigatos, Enhancing induction machine fault detection through machine learning: Time and frequency analysis of vibration signals, *Measurement* 242 (2025) 116023.

[37] T. Sinmazçelik, E. Avcu, M.Ö. Bora, O. Çoban, A review: Fibre metal laminates, background, bonding types and applied test methods, *Mater. Des.* 32 (7) (2011) 3671–3685.

[38] W. Yang, G. Yan, E.M. Awwad, M. Al-Razgan, AI-based solution on the efficient structural design of the graphene-platelets reinforced concrete ceilings, in: *Mechanics of Advanced Materials and Structures*, 2023, pp. 1–24.

[39] T. Liu, A. Wang, Q. Wang, B. Qin, Wave based method for free vibration characteristics of functionally graded cylindrical shells with arbitrary boundary conditions, *Thin-Walled Struct.* 148 (2020) 106580.

[40] N.V. Nguyen, K.Q. Tran, D.T.T. Do, C.H. Thai, K.K. Żur, H. Nguyen-Xuan, An isogeometric analysis of solar panels with a bio-inspired substrate, *Eng. Anal. Bound. Elem.* 166 (Sep. 2024) 105854, https://doi.org/10.1016/j.enganabound.2024.105854.

[41] Y. Qu, X. Long, G. Yuan, G. Meng, A unified formulation for vibration analysis of functionally graded shells of revolution with arbitrary boundary conditions, *Compos. B Eng.* 50 (2013) 381–402.

[42] S. Sun, D. Cao, Q. Han, Vibration studies of rotating cylindrical shells with arbitrary edges using characteristic orthogonal polynomials in the Rayleigh–Ritz method, *Int. J. Mech. Sci.* 68 (2013) 180–189.

[43] B. Qin, K. Choe, Q. Wu, T. Wang, Q. Wang, A unified modeling method for free vibration of open and closed functionally graded cylindrical shell and solid structures, *Compos. Struct.* 223 (2019) 110941.

[44] T. Ye, G. Jin, S. Shi, X. Ma, Three-dimensional free vibration analysis of thick cylindrical shells with general end conditions and resting on elastic foundations, *Int. J. Mech. Sci.* 84 (2014) 120–137.

[45] S. Meng, R. Zhong, Q. Wang, X. Shi, B. Qin, Vibration characteristic analysis of three-dimensional sandwich cylindrical shell based on the Spectro-Geometric method, *Compos. Struct.* 327 (Jan. 2024) 117661, https://doi.org/10.1016/j.compstruct.2023.117661.

[46] J.L. Sewall, E.C. Naumann, *An experimental and analytical vibration study of thin cylindrical shells with and without longitudinal stiffeners*, National Aeronautic and Space Administration 4705 (1968).